

Orleans, June 24th 2020



Dr. Laurent Guillou-Frottier
BRGM, Georesources Division
5 3 av C. Guillemin
BP36009, 45060 Orléans Cedex 2, France

10

Dear Editor,

15

Please find below the two author's comments to the two reviews., as well as a maked-up version of the manuscript (revised manuscript with tracked changes) First review dealt only with english corrections. Second review was more demanding, although the manuscript was favorably received.

We have answered to all comments. Figure 1 has been slightly modified following one remark from R2 (surface heat flow values are now indicated) and equation (A3) has been corrected.

We hope that our revised manuscript will be in a correct form for publication in the Special Volume of Solid Earth.

20

Sincerely Yours,

Laurent Guillou-Frottier and all co-authors

25

File « se-2020-48-AC1.pdf

Dear Editor,

We would like to thank Reviewer 1 for his comments, english corrections and constructive remarks. All
30 suggestions have been accounted for. Since there was no critical points, we simply followed advices from R1.
Some examples are listed below.

Line 34 : « significant, deep » has been added

Line 167 : We agree that a comparison between different density laws could be interesting, but it was not the
scope of this study.

35 Lines 288-291 : we agree that these sentences are not essential and we have deleted them.

Line 384 : One sentence about the observed flow reversal has been added.

Line 464 : R1's suggestion about a transition sentence has been accounted for. We followed his proposition.

Line 467 : « heat advection » has been added.

Line 521 : References to volcanic massive sulfide deposits and to Coumou et al. (2009) have been added.

40 Line 533 : « fluent-rich » has been removed.

Line 557 : « spanning » replaces « including »

Lines 600-601 : Sentence and related references have been removed.

Apart from these minor revisions, the equation A3 has been corrected and an additional funding resource has
been added in the Acknowledgement section.

45

50 Dear Editor,

We would like to thank Reviewer 2 for his comments and his constructive remarks. Each comment or question has been considered. Please find below a point-by-point reply to all comments.

Line 162 : Constant P at the top, so the model is "open-top". Right? What is the T° conditions? constant
55 $T=T(\text{top})$, or $T=T(\text{top})$ when the fluid moves down and $dT/dz(\text{top})=0$ when it is moving up?

→ Yes pressure is fixed at the top, the model is « open-top » . Temperature is fixed at the top boundary, as explicitly written line 160. Boundary conditions are exactly the same as those of Rabinowicz et al. (1998), as explained line 159.

60 Line 172 : When increasing the permeability (or equivalently Ra), the flow dynamics goes through a series of bifurcations starting from steady-state flow

→ We agree with this remark which does not however require any change in the text.

Line 186 : One should consider plotting/giving the heat flux transported by these flows (e.g., the Nu at the base,
65 or the mean flux at the top and/or the flux carried by the individual plumes). That would make sense for a geothermal exploration perspective, especially later in the paper, when more realistic (3D,fracture) geometries are considered.

→ We partly agree with R2. Indeed, most of studies on hydrothermal convection in oceanic crust describe convective patterns and heat flux carried out by thermal plumes. However, in the context of
70 geothermal studies, temperature is much more relevant than heat flux. For example, heat refraction effects could lead to anomalously high heat flux while temperature would not be affected (e.g. Guillou-Frottier et al., Geophys. Res. Lett., 1996). Nonetheless, in the frame of the benchmark tests of Fig. 1, the maximum heat flux carried by thermal plumes is now indicated. The obtained values are similar to the results published by Rabinowicz et al. (1998). Note that spatial evolution of surface heat flux has already
75 been published by Garibaldi et al. (2010), their Fig. 10, and numerical values compared well with the results of Rabinowicz et al. (1998).

Line 194 : Are all these simulations steady-state? I would have thought that at least at 10-13m², the flow is not steady anymore? How does this compare with other code (Rabinowicz, Fontaine, Coumou...)

80 → Yes, as indicated in the caption, these simulations are all steady-state, or show a steady-state pattern after a transient stage. As noted in the last sentence, « *Above 10^{-13} m^2 , convection exhibits unsteady patterns, including typical Y-shaped and splitting plumes.* ». These results are identical to those of Rabinowicz et al. (1998), as written line 192.

85 Line 217 : I think that the reduction of the number of plumes have a lot to do with the fact that the local Ra at the base of the system is much smaller than at the top, and that accordingly less plumes arise in the thermal boundary layer at the base.

90 → We completely agree with R2's remark, which is another way to explain the physical mechanism. It is exactly the same as our explanations, but expressed with the local Rayleigh number instead of local permeability (our choice).

Line 240 : What is the heat flux (mean and /or individual/plumes) doing?

95 → We have added in the text the time evolution of surface heat flux carried out by thermal plumes (right before Fig. 3), but here again, in the frame of geothermics, temperature anomalies are more relevant for exploration. In addition, informations are given for the top surface and not at the base of the system since geothermal exploration is more interested in shallow thermal anomalies.

100 Line 258 : Again here, a plot showing the temporal variation of the mean heat flux (e.g., the Nu at the base of the system) would be useful to understand this pattern. When the permeability starts to increase is the flux decreasing, or increasing?

→ When permeability starts to increase, the surface heat flux over the plume head increases from 5 to 35 W.m^{-2} during the first 200 years. This is now specified in the text (lines 262-263).

105 Line 321 : I don't think this is actually, "plume splitting", more "plume pulsating". Plume splitting as described by Coumou and also by Fontaine, is a dynamical phenomena occuring when a hot rising plume meets a cold downwelling (or stagnant) front and the plume splits in several finger-like structures. Coumou has explained this phenomenon which requires a threshold plume velocity and a viscosity contrast. Coumou also explains that high-order in time and space numerical schemes (and low spatial resolution too) is necessary to see this. What I see on figure 7 here, is the pulsation of the plume because the lower thermal boundary become unstable (see the plumelets). In Fontaine&Wilcock 2007, we have highlighted and described this behavior (including periodicity) which is characteristics when the permeability exceeds c.a. 10^{-14} m^2 . The authors should distinguish carefully these 2 phenomena (i.e., pulsation vs. splitting). I am surprised to see that some of the models in figure 1 are steady, while the permeability is $>10^{-14} \text{ m}^2$. So I have 2 questions: 1- how accurate is the scheme, and maybe it would be worth reproducing basics Ra-Nu relationships (see benchmark table in

115

Fontaine&Wilcock 2007 for example); 2- Do you see actual "plume splitting"? I attached a figure from Coumou showing plume splitting.

- We thank R2 for this relevant remark. The word « pulsating » is indeed more appropriate and « splitting » is now changed by « pulsating ». Reference to Fontaine & Wilcock (2007) has been added and the obtained similar timescales are underlined. Details on the numerical procedure (accuracy, tolerances, type of solver) have already been given at the end of Appendix A. It is also well-known that different solutions can be obtained with different numerical codes, as discussed in Appendix B.
- Yes, actual plume splitting was also observed at permeability values exceeding 10^{-13} m², as indicated at the end of the caption of Figure 1 (we refer to this mechanism as « *Y-shaped and splitting* » plume).

Line 340 : What are the initial conditions in these models? In 2D you argue that the initial condition was important for the final flow geometry. Is it the case in 3D?

- We thank R2 for this question. Indeed, initial conditions may influence the following convecting pattern, as observed and demonstrated in 2D models. However, for all 3D models, the initial condition was a purely conductive regime, an information that was not clear. This is now specified line 384.

Line 363 : What if it does ?

- We did not investigate all possible configurations. We chose to look at non-outcropping fault zones. Tests on outcropping fault zones would correspond to another entire study.

Line 373 : How do you deal with the flow in the fracture and in the rocks around? Is the flow (i) 3D everywhere and you just have a permeability contrast between the fracture and the rocks or (ii) do you have "fracture flow" in 2D in the fracture and 3D in the rocks around. If you do (i) then you should discuss somewhere what is the limitations of that with respect to a more realistic "fracture flow". Maybe some insights in Mezon et al. 2018 (*Physical Review E*, 97(1), 013106.)

- Answer is (i) : the flow is 3D everywhere, but the low permeable host rocks do not involve significant fluid flow around the fault. We have added 2 sentences at the beginning of the discussion to not ignore the « fracture flow » approach, which is not necessarily more « realistic » than our approach in the case of crustal fault zones, whose thickness may reach hundreds of meters. This is now specified and reference to Mezon et al. 2018 has been added.

Line 385 : I can see that in all the inclined models, the temperature perturbation follows the dip of the fault. In the 2D models of Andersen et al. 2015 (*Geology* (2015) 43 (1): 51–54.) there is a discussion about the fact that there is a competition between the buoyancy of the fluid that tend to favor purely vertical flow, and the dip angle. For example sometimes in Andersen et al 2015, the flow follows the fault plane at depth and then turn to vertical at shallow depth. You don't seem to observe that? Why (2D vs. 3D, boundary conditions?) It may have

to do with the fact that your host rock is "impervious" with $K_h=1e-18m^2$, but what if you consider an inclined fault models with depth-dependent permeability and for which the K_f/K_h ratio is "small" (i.e., the permeability of the host rock is not small at shallow depth, like in figure 14, but with an inclined fault).

155 → We thank Reviewer 2 for letting us know about this Andersen et al. Paper. Comment by R2 is interesting, and his answer is right : indeed, host rocks are almost impervious, preventing fluid flow to turn to the vertical at shallow depth. However, we could not test all possible k_f/k_h ratios, but we believe that Fig. 14 allows considering its effect on convective patterns. These tests would be worth to investigate in a future study.

160

Line 529 : « fluent-rich » ?

→ These precision has been removed.

Line 598 : In your models in which this ratio is 20 (or 50), don't you get thermal instabilities in the host rock rather than only along the fault plane? I anticipate that in a 5.5km-deep system the effective Ra of the host rock could be supercritical if that ratio is "small" like 20. I guess it also depends on your depth-dependent permeability distribution, but you may have a completely different flow geometry if plumes start to arise in the host rock.

170

→ We definitely agree with Reviewer 2. However, our objective was not to make a complete sensitivity study on all parameters. Many simulations would be needed to answer to this remark, and this was not the aim of our work, as underlined in the abstract (« *This study presents a non-exhaustive numerical investigation...* »).

Line 612 : Could you show a figure in which you calculate the volume (m^3) of the thermal anomalies for the 3D models? as a function of ΔT , or for a ΔT greater than a predefined value that would have a geothermal meaning? This would be interesting to size the potential of geothermal energy.

175

→ This is actually planned for the next step of our approach. We first presented « simplified models » to illustrate some mechanisms. Because a number of simplifications have been chosen, it would not be reasonable to « size the potential of geothermal energy ». However, such estimate is currently worked in the frame of Duwiquet's PhD thesis (second author), who applies this approach to the natural system of the Pontgibaud crustal fault zone, French Massif Central (Duwiquet et al., 2019).

180

Laurent Guillou-Frottier and all co-authors

185

Following pages : Revised manuscript with tracked changes

190

On morphology and amplitude of 2D and 3D thermal anomalies induced by buoyancy-driven flow within and around fault zones

Laurent Guillou-Frottier^{1,2}, Hugo Duwiquet^{1,2,3}, Gaëtan Launay⁴, Audrey Taillefer⁵, Vincent Roche⁶, Gaëtan Link⁷.

195 ¹BRGM, Georesources Division, 45060, Orléans, France

²ISTO, UMR7327, Université d'Orléans, CNRS, BRGM, 45071 Orléans, France

³TLS-Geothermics, 31200, Toulouse, France

⁴Laurentian University, P3E2C6, Sudbury, Canada

⁵CFG Services, 45060, Orléans, France

200 ⁶ISTEP, UMR7193, Sorbonne Université, CNRS-INSU, 75005, Paris, France

⁷GET, UMR 5563, Université Toulouse III-Paul Sabatier, CNRS, IRD, CNES, 31400, Toulouse, France

Correspondence to: Laurent Guillou-Frottier (l.guillou-frottier@brgm.fr)

Manuscript submitted to *Solid Earth*, April 10, 2020

205 Special Issue: "Faults, fractures, and fluid flow in the shallow crust »

Abstract.

In the first kilometres of the subsurface, temperature anomalies due to heat conduction processes rarely exceed 20-30 °C.

When fault zones are sufficiently permeable, fluid flow may lead ~~to much larger~~ thermal anomalies ~~much higher~~, as evidenced by the emergence of thermal springs or by fault-related geothermal reservoirs. Hydrothermal convection triggered

210 by buoyancy effects creates thermal anomalies whose morphology and amplitude are not well known, especially when depth- and time-dependent permeability are considered. Exploitation of shallow thermal anomalies for heat and power production partly depends on the volume and on the temperature of the hydrothermal reservoir. This study presents a non-exhaustive numerical investigation of fluid flow models within and around simplified fault zones, where realistic fluid and rock properties are accounted for, as well as appropriate boundary conditions. 2D simplified models point out relevant physical mechanisms

215 for geological problems, such as "thermal inheritance" or ~~splitting-pulsating~~ plumes ~~showing a pulsating behaviour~~. When permeability is increased, the classic "finger-like" upwellings evolve towards a "bulb-like" geometry, resulting in a large volume of hot fluid at shallow depth. In the simplified 3D models, where fault zone dip angle and fault zone thickness are varied, the anomalously hot reservoir exhibits a kilometre-sized "hot air balloon" morphology, or, when permeability is depth-dependent, a "funnel-shape" geometry. For thick faults, the number of thermal anomalies increases but not the amplitude. The largest amplitude (up to 80-90°C) is obtained for vertical fault zones. At the top of a vertical, 100 m wide, fault zone, temperature anomalies greater than 30°C may extend laterally over more than 1 km from the fault boundary. These preliminary results should motivate further geothermal investigations of more elaborated models where topography and fault intersections would be accounted for.

1. Introduction

225 In the shallow crust, several geological systems meet the necessary conditions for the occurrence of significant, deep, fluid circulation. Tectonically active systems, ash-flow calderas, sedimentary basins and especially crustal fault zones correspond to dynamic systems which are sufficiently porous and permeable to host fluid circulation (e.g. Simms and Garven, 2004; Hutnak et al., 2009; Lopez et al., 2016; Patterson et al., 2018a ; Duwiquet et al., 2019). As soon as rock permeability is large enough, meteoric, metamorphic or magmatic fluids can flow along kilometer-scale pathways, at velocities reaching up to
230 several meters per year (e.g. Forster and Smith, 1989 ; Lopez and Smith, 1995). When fluid velocity is sufficiently large, heat can be advected with the fluid to shallow crustal levels (e.g. Ague, 2014), leading to the development settlement of hydrothermal reservoirs and thus to exploitable thermal anomalies. Similarly, when cold fluid is transferred to deep levels (or when deep hot fluids rise in the intermediate crust), precipitation of minerals can be favored and mineralizing processes may form exploitable ore deposits (e.g. Fehn et al., 1978 ; Boiron et al., 2003 ; Weis et al., 2012). Whether geothermal resources
235 or mineral resources are targeted, the main questions that have generally to be solved deal with the location and with the volume of the reservoir. This study is focused on the « geothermal side » of hydrothermal resources (i.e. mineralizing processes are not considered) and particularly on the formation of anomalously hot and shallow hydrothermal reservoirs.

In shallow permeable zones, at the scale of kilometer-sized reservoirs, two main processes can control fluid circulation: (i)
240 significant pressure gradients, which can result from an important topography or from magmatic or metamorphic fluid production, and (ii) buoyancy effects, due to temperature-dependent fluid density, that can result in thermal convection in permeable media. In the first case, the term « forced convection » is employed while in the second case, « free convection » is used. Although both processes can occur at the same time (see for example the numerical models of the Basin and Range extensional geothermal systems, by McKenna and Blackwell, 2000), one of the two convection modes may predominate. For
245 example, in the case of an important significant topography (1000 – 2000 m), forced convection may control the fluid flow regime as in the case of Alpine hydrothermal systems (e.g. Sonney and Vuataz, 2009). However, in the case of a fault zone with a high permeability, free (thermal) convection may prevail over forced convection.

The possibility for thermal convection to occur within a permeable medium was often tested with the calculation of the
250 Rayleigh number (e.g Turcotte and Schubert, 2002). This dimensionless number depends on the imposed temperature gradient, on the considered geometry and on fluid and rock properties. If the Rayleigh number exceeds a critical value, then thermal convection occurs. The critical value of $4\pi^2$ (Lapwood, 1948) was determined by linear stability analysis for an infinitely long homogeneous porous medium, where fixed temperature conditions are applied on both horizontal boundaries, and for a constant viscosity fluid. For different (and more realistic) boundary conditions (e.g. fixed heat flow at depth and fixed pressure
255 at the surface) the critical Rayleigh number is decreased (see Jaupart and Mareschal, 2011). When temperature-dependent viscosity is accounted for, Lin et al. (2003) demonstrated that the critical Rayleigh number is also decreased when compared

to the constant viscosity case. In other words, when realistic boundary conditions are considered and when appropriate fluid properties are taken into account, the critical permeability for which free convection would occur is not as high as previously thought.

260

In the case of a finite size vertical fault zone, Malkovski and Magri (2016) developed a new linear stability analysis accounting for temperature-dependent fluid viscosity. They showed, in accordance with Wang et al. (1987), that the critical Rayleigh number can be expressed with the fault aspect ratio (half-width over depth), but also with a dimensionless thermal parameter describing the temperature-dependence of the fluid viscosity. One of their conclusions is that the Rayleigh theory may not be sufficient when fluid properties are adequately considered. In addition, the critical permeability for which free convection develops may be four times lower than initially predicted within the constant viscosity hypothesis. One limit of their theoretical study lies however in the investigated temperature range, limited to a domain where a linear fit to density variation holds. Indeed, for temperatures greater than 300°C, the linear fit does not hold anymore, and one must thus refer to a numerical approach where an appropriate density law (non-linear, pressure- and temperature-dependent) can be accounted for.

270

In this study, we focus on hydrothermal convection that could lead to the establishment of exploitable thermal anomalies. Geothermal resources leading to power production generally require temperatures higher than 150°C, and present-day exploration projects tend to target supercritical conditions, involving much higher temperatures (« high enthalpy geothermal systems » or, as recently suggested, « superhot geothermal systems »; e.g. Scott et al., 2015; Watanabe et al., 2019), in particular around the brittle-ductile transition (350-400°C, Violay et al., 2017). It is thus necessary to study hydrothermal convection where temperature can exceed 300°C, a domain for which fluid properties are highly nonlinear. For example, Jupp and Schultz (2000) demonstrated that the surprising constant temperature of black smokers (around 380°C) could be explained by the maximization of the « fluxibility » parameter, which depends on thermodynamic properties of water (density, viscosity and specific enthalpy).

280

Besides accounting for appropriate fluid properties, studies on hydrothermal convection need to consider realistic rock permeability. This physical property, initially supposed to be « static », has been more and more considered as « dynamic », not only through field and petrologic observations (e.g. Jamtveit et al., 2009 ; Faulkner et al., 2010 ; Stober and Bucher, 2015) but also in numerical models and laboratory experiments (Tenthorey and Cox, 2003; Tenthorey and Fitzgerald, 2006; Coelho et al., 2015; Ingebritsen and Gleeson, 2015 ; Mezri et al., 2015 ; Weis, 2015 ; Launay et al., 2019). Several mechanisms can explain spatial (e.g. depth-dependent) and temporal (e.g. stress-dependent) variations of permeability. For example, fluid-rock interactions may involve mineralogical transformations leading to continuous increase of permeability (Launay, 2018). A gradual permeability increase in a fault damage zone has been suggested by Louis et al (2019) to explain temporal evolution of the Beowawe hydrothermal system in Nevada. However, depending on the hydrogeologic and tectonic setting, sudden increase or decrease of permeability could also happen and should significantly affect the fluid flow conditions. ~~If~~ Whereas

290

the effect of heterogeneous and dynamic permeability has already been studied around magmatic intrusions (e.g. Gerdes et al., 1998 ; Weis et al., 2012 ; Scott and Driesner, 2018 ; Launay, 2018), this is not the case for fault zones.

295 This study is intended to show, with a numerical modeling approach, how hydrothermal convection establishes in a permeable
fault zone, how convective patterns are organized, and which kind of particular phenomena can be observed. The effects of
topography are not accounted for in this preliminary approach. First, 2D numerical models are presented, with constant, depth-
dependent and time-dependent permeability. The effects of ~~a~~-variable permeability are discussed in terms of convective
patterns and temperature distribution (morphology and amplitudes of thermal anomalies). Finally, simple 3D numerical models
of hydrothermal convection in permeable fault zones illustrate how positive thermal anomalies can establish at shallow depths,
300 thereby illustrating an interesting predictive tool for geothermal exploration, where maps of temperature anomalies often
~~influence drilling strategies correspond to the first major information~~ (e.g. Clauser and Villinger, 1990 ; Bonté et al., 2010 ;
Garibaldi et al., 2010 ; Guillou-Frottier et al., 2013).

2. Typical structural settings and permeability values for hydrothermal systems

~~Apart from geothermal systems associated with a magmatic heat source which drives excess heat toward shallow depths, fault~~
305 ~~Fault~~ zones may serve as efficient conduits for deep hot fluids to rise up to the surface (e.g. Curewitz and Karson, 1997; Fairley
and Hinds, 2004; Person et al., 2012; Bense et al., 2013; Sutherland et al., 2017). Faulds et al. (2010) analyzed different
geothermal systems in back-arc domains (Nevada and western Turkey) and concluded that specific structural settings were
involved in the localization of geothermal systems. Discrete steps in normal fault zones, terminaisons of major normal faults,
or fault stepovers (among other fault features) appear to control locations of the investigated geothermal systems. On the basis
310 of field studies in western Turkey, Roche et al. (2019) suggested that the intersection between crustal-scale low-angle normal
faults and transfer faults represents the first-order control on geothermal systems.

Fault stepovers have also been suggested to control the location of supergiant gold deposits (Micklethwaite et al., 2015), which
correspond to fossil hydrothermal systems. According to the authors, formation of supergiant gold deposits would be associated
315 to transient variations of permeability, whose value may reach 10^{-12} m². Person et al. (2012) modelled hydrothermal fluid flow
at intersections of 10–20 m wide fault zones. They reproduced typical hydrothermal activity of the Basin and Range extensional
tectonic province with permeability values between 5 and $7 \cdot 10^{-13}$ m². Such high permeability values were also proposed in
low-temperature active geothermal systems (e.g. Truth and Consequences geothermal system in New Mexico, Pepin et al.,
2015).

320 When larger fault zones are considered, smaller permeability values are inferred. According to recent studies on different
geological systems, it seems that permeability greater or around 10^{-14} m² could represent a typical value for which geological

data can be reproduced. For example, in the case of the 300 m wide Têt fault system, French Pyrenees, Taillefer et al. (2018) reproduced locations and temperatures of the 29 thermal springs with a permeability value of 10^{-14} m². In a 3D model of the Lower Yarmouk Gorge, at the border between Israel, Jordan and Syria, Magri et al. (2016) also reproduced clusters of thermal springs with realistic temperatures, with a fault permeability of $2.3 \cdot 10^{-14}$ m². Roche et al. (2018) qualitatively reproduced temperature profiles measured within fault-related geothermal systems in western Turkey when permeability of detachments (low-angle normal faults, 200–400 m wide) equals 10^{-14} m². When fault permeability is higher, cold downwellings may be favored within the fault, as in the numerical simulations of the Soultz-sous-Forêts geothermal system where fault width equals 100 m (Guillou-Frottier et al., 2013). In the case of the Pontgibaud crustal fault zone (French Massif Central), Duwiquet et al. (2019) reproduced present-day surface heat flow and temperature gradient for a maximum permeability of $1.6 \cdot 10^{-14}$ m², a value for which a high temperature (150°C) hydrothermal reservoir could ~~settle-occur~~ at a depth of 2.5 km. ~~It may be worth to~~ This result suggests considering the possibility of a critical fault permeability above which positive thermal anomalies disappear in favor of negative anomalies, but Lopez and Smith (1995) ~~already~~ showed that the role of host rock permeability has also to be taken into account (see also Della-Vedova, 2008). ~~In addition, the~~ The permeability ratio between fault zone and host rocks may ~~be correspond to~~ one critical parameter for building a convective regime diagram, as suggested by Duwiquet et al. (2019). Consequently, the complex coupling between host rock and fault zone permeability will be also considered in this study.

3. Method

All numerical simulations presented in this study correspond to ~~the~~ coupling of the heat equation with ~~the~~ Darcy's law, while mass conservation is applied. We used the Comsol Multiphysics™ software, ~~by~~ computing transient evolution of hydrothermal convection lasting, in some cases, up to several hundreds of thousands years. In the more elaborated experiments (3D geometry), fluid density is temperature- and pressure-dependent, and fluid viscosity is temperature-dependent. Governing equations are detailed in Guillou-Frottier et al. (2013). Physical laws and numerical procedure are detailed in Appendix A. We restrict our study to the (P,T) domain where fluid stays in a ~~fluid-liquid~~ phase (i.e. no vapor phase), as for example in the case of pure water at 350°C at 2-3 km depth.

Before performing 3D simulations of hydrothermal convection in fault zones, 2D experiments are presented in order to highlight and review how convective patterns are organized in a permeable medium, where permeability is progressively constant, depth-dependent and time-dependent. The first 2D simulations (Fig. 1 to Fig. 7) are based on the same set-up, boundary conditions and physical properties as those used by Rabinowicz et al. (1998). A 1.5 km-thick and 4.5 km-wide permeable medium is thermally insulated on both vertical sides. Fixed temperature conditions of 0°C and 400°C are imposed on top and bottom boundaries, respectively. A no flow condition is imposed on all boundaries except on the top one, where a fixed pressure of 10^5 Pa is present (Fig. 1a).

355 The second series of numerical experiments deal with 3D models of hydrothermal convection in a fault zone embedded in low
permeable-permeability host rocks. Benchmark tests are performed in order to reproduce the already-published results by Magri
et al. (2017). For these particular 3D benchmark tests (detailed in Appendix B), a simplified density law (linear decrease with
temperature) is-was imposed by the Magri et al. (2017) study. In the other 3D simulations (Fig. 8 to Fig. 14), a more realistic
pressure- and temperature-dependence for fluid density is used, and a more realistic thermal boundary condition is applied at
360 the bottom boundary (a fixed heat flow condition). One of the objectives of these 3D models is to understand how and where
thermal anomalies develop. The role of the dip angle of the fault zone is tested, as well as the role of permeability distribution
within the model.

4. Results from 2D models

4.1 Constant permeability

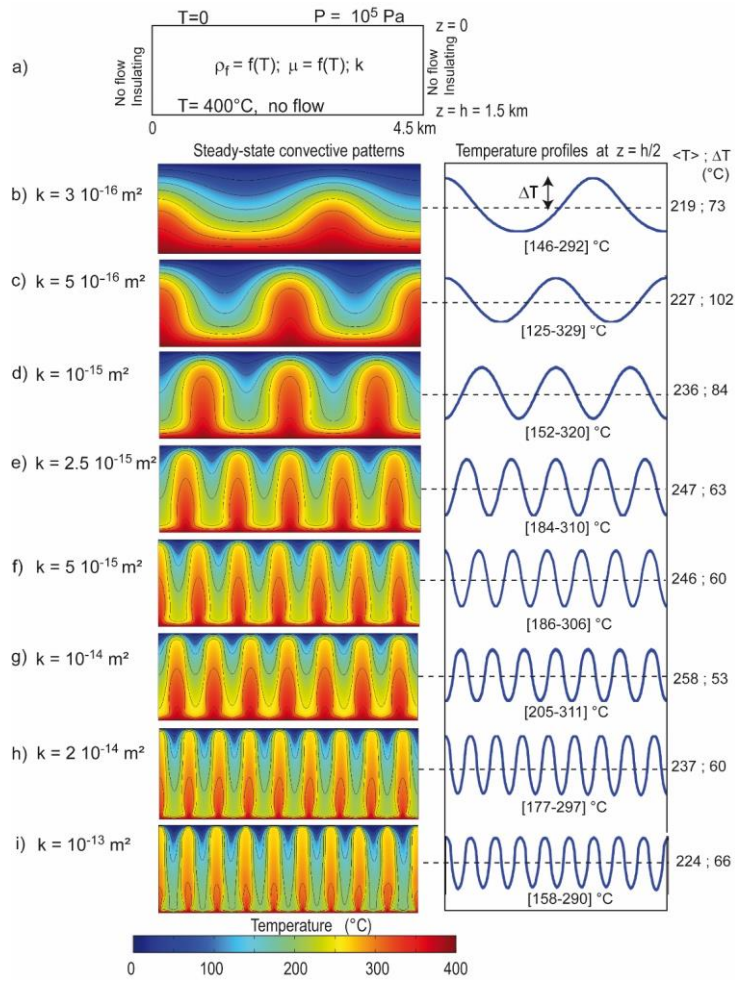
365 Figure 1 illustrates hydrothermal convection for constant permeability values, from the onset of thermal convection (Fig. 1b)
to vigorous convection, just before unsteady or turbulent convective patterns dominate. As already shown by many studies
(e.g. Rabinowicz et al., 1998) the vigor of thermal convection (or the number of upwellings, or the maximum fluid velocity
value) increases with a-permeability-increase. Convective wavelength decreases with a-permeability-increase, and up to 8
internal upwellings (i.e. without considering the half plumes at lateral boundaries) are obtained in the most permeable case
370 (10^{-13} m², Figure 1i). While changes in the convective patterns are understandable (the more permeable is the-medium, the
more active is-the convective regime), the evolution of thermal characteristics is less obvious. The right column in Fig. 1 shows
horizontal temperature profiles at mid-depth, with numerical values of the horizontally-averaged temperature $\langle T \rangle$, and-of
the temperature excess ΔT compared to this average and the maximum heat flux (Φ_{max}) carried by thermal plumes at the top
surface. This later values are in accordance with the results of Rabinowicz et al. (1998), as well as spatial variation of surface
375 heat flux (see also Garibaldi et al., 2010). It must be noted that dueDue to asymmetric flow conditions at horizontal boundaries
and non-linear fluid properties, the averaged temperature at mid-depth exceeds 200°C, the temperature that would be present
in the purely conductive case-with no heat source. When thermal convection occurs, this horizontally-averaged value of 200°C
can be obtained at mid-depth if fluid density varies linearly with temperature and when a no flow condition – as at bottom
boundary – is imposed on the top surface.

380

Finally, Fig. 1 shows that while permeability increases, the increase of the horizontally averaged value $\langle T \rangle$ is not regular, as
well-as nor is the temperature excess ΔT . Similarly, the minimum and maximum temperatures reached at mid-depths (values
in brackets below horizontal temperature profiles) do not evolve regularly-from top to bottom experiments. The obtained
convective patterns in Fig. 1 will be named in the following as-called « finger-like » upwellings as in, e.g., Zhao et al (2003),
385 with almost vertical isotherms bounding upwellings and downwellings, as also illustrated by Rabinowicz et al. (1998).

Mis en forme : Police :Symbol

Mis en forme : Indice



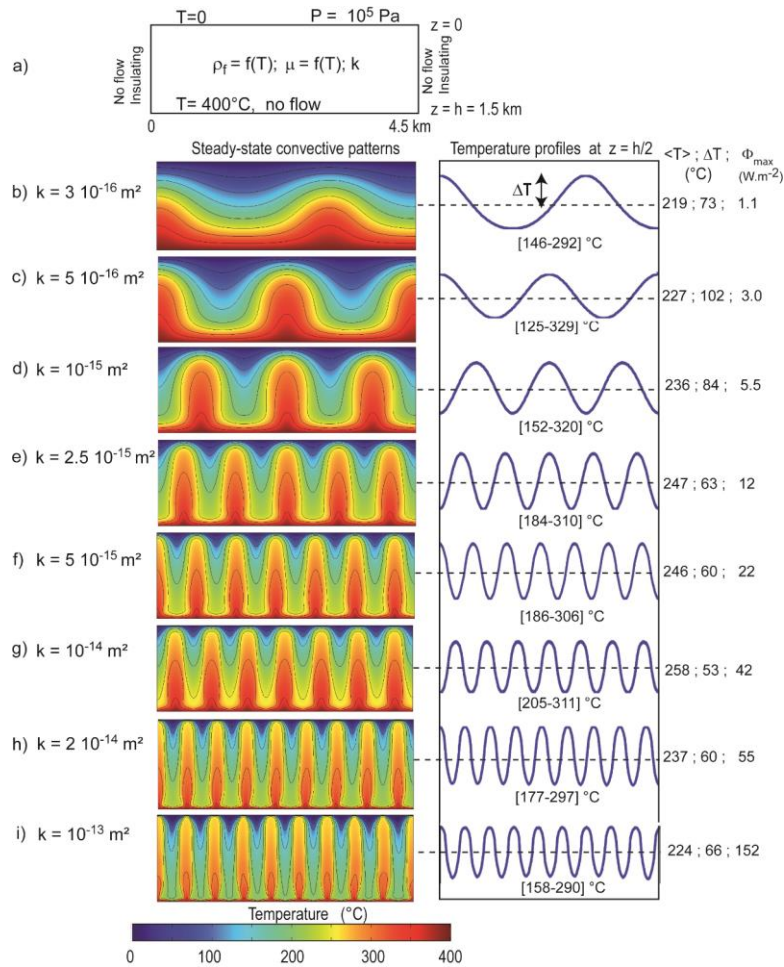
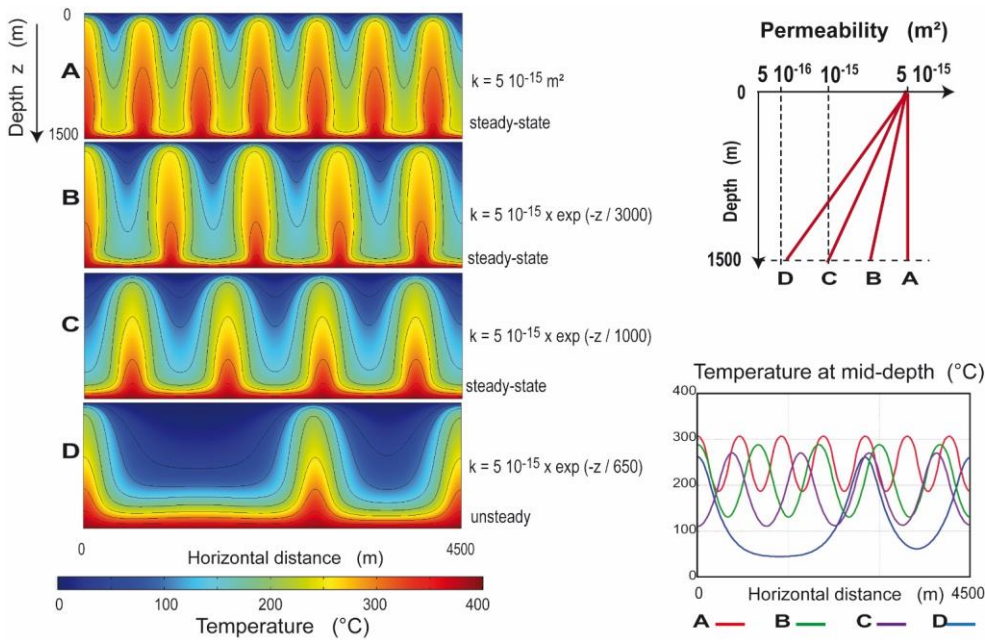


Figure 1: Steady-state temperature fields obtained for different values of the medium permeability. Left column shows temperature fields and right column illustrates a horizontal temperature profile at mid-depth. Averaged temperature at mid depth ($\langle T \rangle$), and temperature anomalies (ΔT) and maximum heat flux carried by thermal plumes at the top surface are indicated on the right of each profile. Numerical set-up and boundary conditions are illustrated in a) and detailed in the text. For all experiments, the maximum mesh element size is 20 m. Hydrothermal convection (b) is observed for permeability around $3 \cdot 10^{-16} \text{ m}^2$ (a pure conductive regime is obtained for smaller permeability). The number of upwellings increases with increasing permeability. Above 10^{-13} m^2 , convection exhibits unsteady patterns, including typical Y-shaped and splitting plumes (see section 4.5).

4.2 Depth-dependent permeability

In the shallow crust (above the brittle-ductile transition), permeability is ~~supposed-expected~~ to decrease with increasing lithostatic pressure (e.g. Manning and ~~IngebristenIngebritsen~~, 1999; Saar and Manga, 2004; Achtziger-Zupančič et al., 2017) but this depth-dependence may be less effective in highly permeable fault zones, like extensional faults in the Larderello and other geothermal systems (Della-Vedova et al., 2008; Scibek, 2020). In the case of a constant pressure boundary condition at the top surface (a more realistic condition for geological systems ~~than when compared to a~~ “no flow” condition), the fact that permeability decreases with depth has important consequences on convective patterns. In Fig. 1, the finger-like upwellings are embedded within their cold counterparts (finger-like downwellings), thus exhibiting a perfect geometrical symmetry. ~~On the opposite~~In contrast, when permeability decreases with depth, the number of upwellings decreases (Fig. 2). Case A corresponds to Fig. 1f, and cases B, C and D illustrate experiments with an exponentially-decreasing permeability with depth. The decrease ~~of in~~ the number of upwellings can be explained by the asymmetric distribution of temperature and permeability: cold fluids are located in the most permeable zones, whereas hot fluids at depth encounter less permeable medium. ~~In other words, fluid flow is facilitated in cold zones.~~ Consequently, cold downwellings are favored and a general cooling is obtained in the last case (see mid-depth temperature profiles in Fig. 2). Contrary to the constant permeability cases, individual upwellings do not show a regular distribution of finger-like upwellings, since the cooling effect in the upper levels dominates and tends to destroy upwelling heads. According to their geometry, these upwellings will be named « triangular-like » upwellings (see in particular the cases C and D).



415 Figure 2. Effect of the depth-dependence (decrease) of the permeability, here taken as exponential. The number of upwellings decreases when the depth-dependence is accounted for: 6 internal upwellings are obtained for the constant permeability case (labelled “A”, top pattern) but only one for the **important-steepest** exponential decrease (“D”, bottom). Horizontal temperature profiles at mid-depth (bottom right) illustrate **a** the major cooling effect, as well as the increasing temperature contrast between upwellings and downwellings when depth-dependence is increased. See text for explanations.

420 **4.3 Time-dependent permeability**

4.3.1 From a depth-dependent to a constant permeability: instantaneous increase

Seismic activity could reactivate former deformation zones and thus **trigger** instantaneously **trigger** a permeability increase (e.g. Sibson, 1992; Cox, 2010). Figure 3 illustrates the modifications of temperature patterns when a sudden increase in permeability is applied to ~~the previous~~ case C of Fig. 2. The depth-dependence of permeability is instantaneously cancelled and a constant permeability of $5 \cdot 10^{-15} \text{ m}^2$ is applied. Because permeability is increased at the bottom of the system, deep hot fluids can move upward more easily, and the triangular-like upwellings evolve toward a « bulb-like » geometry, with a shrinking tail and a large head. Surprisingly, the convective pattern illustrated in Fig. 1f (permeability of $5 \cdot 10^{-15} \text{ m}^2$) – i.e. with

finger-like upwellings – is not recovered, although permeability is the same. Actually, the initial thermal regime in the first case (Fig. 1f) corresponds to a conductive regime whereas in Fig. 3, the initial regime corresponds to the triangular-like geometry. Similar observations are described in section 4.4. This could be explained by the different initial thermal regimes, as detailed in section 4.4.

Another interesting feature deals with the thermal anomalies that are generated by those bulb-like upwellings. Figure 3 shows that the instantaneous increase in permeability has a warming effect at a depth of 600 m and a cooling effect at a depth of 1300m. The warming effect corresponds to the larger head, and the cooling effect to the shrinking tail. When compared to the preexisting case of triangular-like upwellings, temperature differences reach, +50°C and -70°C, respectively (bottom plots of Fig. 3). Heat flux at the top surface increases regularly from 8 to 17 W.m⁻² during 6000 years before reaching steady-state.

Mis en forme : Exposit

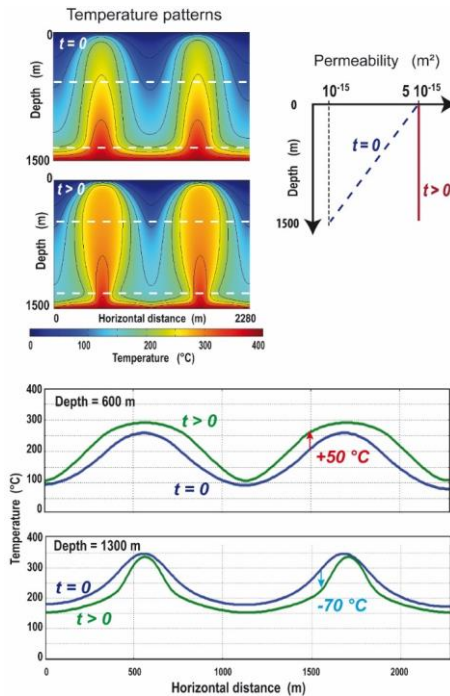


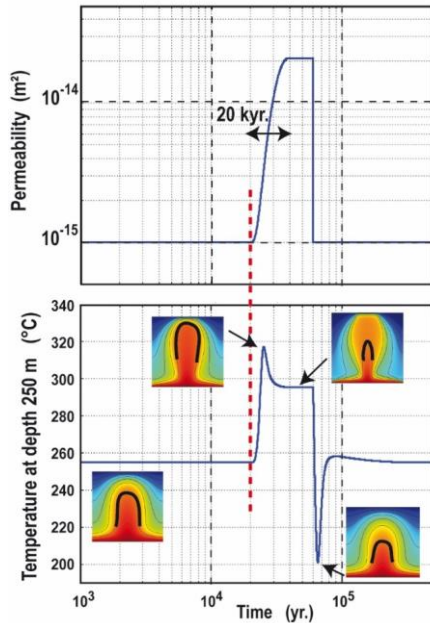
Figure 3. Effect of a sudden increase of permeability: from a depth-dependent variation (dashed line in the top-right plot) to a higher constant permeability (red line). Temperature patterns (top left) show that the initial « triangular-like » geometry (t=0) of the upwellings evolves toward a « bulb-like » geometry. Lower plots show the temperature variations along the white dashed lines illustrated in the temperature patterns. Bulb-like regime involves higher positive temperature anomalies in the upper part of the system (up to 50°C), and higher negative temperature anomalies in the lower part (down to -70°C).

445 **4.3.2 From a constant to a higher permeability: time-dependent increase**

450 ~~Contrary to an instantaneous increase, a~~ progressive increase of permeability could be related to fluid-rock interactions that ~~could~~ trigger the dissolution of ~~some~~ minerals like quartz and calcite. This dissolution induces porosity generation which in turn increases permeability (Scott and Driesner, 2018; Launay et al., 2019). One could also invoke tectonic processes like regional uplift which modifies pressure conditions that partly control permeability. ~~On the opposite~~In contrast, progressive mineral deposition in the permeable structure can ~~seal the deformation zone, resulting~~ in a permeability decrease (e.g. Lowell et al., 1993). Figure 4 illustrates the effects of a non-instantaneous increase of permeability for an initial convective pattern corresponding to a finger-like geometry (constant permeability of 10^{-15} m², case of Fig. 1d). Here, a permeability increase by a factor 20 is imposed over a total duration lasting 20 kyr (see top plot in Fig. 4). This arbitrarily chosen duration allows ~~identification of~~ying a transient unexpected warming event, highlighted by an increase in surface heat flux over the plume head, from 5 to 35 W.m⁻² during 200 years, and reaching steady-state at 33 mW.m⁻² in which occurs in the first 10 kyr, in accordance with ~~These timescales are similar to~~ seismically-induced fault permeability changes described by Howald et al. (2015).

Mis en forme : Expositant

Mis en forme : Expositant



460 **Figure 4.** Effect of a time-dependent permeability, increasing by a factor of 20 in 20 kyr. The finger-like geometry (lower left pattern) evolves towards a bulb-like geometry (upper right pattern). Temperature profile (bottom plot) shows short-duration heating and cooling events. The thick black contour on convective patterns corresponds to the 300°C isotherm. . Color-bar (not shown) is the same as in previous figures.

465 ~~Indeed, when~~When permeability increases, hot fluid moves upward more easily, thus creating a warming effect at shallow depth, from $t = 2.0 \cdot 10^4$ yr. to $2.5 \cdot 10^4$ yr. (see temperature evolution at a depth of 250 m, in the bottom plot). As illustrated by colored patterns in Fig. 4, this first phase corresponds to the transition from a finger-like to a bulb-like pattern. After $2.5 \cdot 10^4$ yr., while permeability is still increasing, a cooling effect dominates, as illustrated by temperature plot and colored patterns, where the thick black line indicates the 300°C isotherm. When permeability is stabilized at $2 \cdot 10^{-14}$ m², temperature becomes stable and the bulb-like pattern does not evolve. At time $t = 6 \cdot 10^4$ yr., ~~the an~~ instantaneous decrease of the permeability toward the initial value of 10^{-15} m² shifts the bulb-like geometry to the expected finger-like geometry. However, ~~it is interesting to note that~~a short-duration important cooling stage (from 295°C to 200°C) occurs during the instantaneous permeability decrease, before the initial finger-like pattern is recovered.

470

4.4 Role of initial thermal regime: thermal inheritance

As illustrated by Fig. 1f and 3, different steady-state convective patterns can be obtained if the initial thermal regime differs: in the case of an initial purely conductive regime, a finger-like geometry is obtained with a permeability of $5 \cdot 10^{-15} \text{ m}^2$ (Fig. 1f), while a bulb-like geometry is obtained when the initial thermal regime corresponds to triangular-like upwellings (Fig. 3). In the following, different initial thermal regimes are considered and the evolving convective patterns are recorded when permeability is instantaneously increased up to a given value, identical for all cases. This type of simulations can illustrate what could happen in active and polyphased geological systems like orogenic belts.

In Fig. 5, initial permeability (hereafter noted k_0 , patterns in the left column) is instantaneously increased to $5 \cdot 10^{-15} \text{ m}^2$. The first experiment in Fig. 5 corresponds to Fig. 1f: starting from a conductive regime (flat isotherms), a finger-like geometry is obtained, with 6 internal upwellings. When the initial thermal regime corresponds to a convective pattern obtained with a permeability of $5 \cdot 10^{-16} \text{ m}^2$, the finger-like upwellings evolve toward a bulb-like geometry (intermediate and final stages), and the number of internal upwellings slightly increases, from 1 (initial and intermediate stages) to 3 (final steady-state). In the last experiment of Fig. 5, the 3 initial upwellings are conserved, and here again, a bulb-like geometry is promoted. Conservation of the initial number of upwellings will be referred in the following to as « thermal inheritance ». ~~In that later case, the final pattern appears to be unstable, with no half upwellings on the sides, as in the previous case. This is probably due to the fact that the box length is not adapted with only 3 upwellings (see Börsing et al., 2017 for discussions on stable convective patterns versus box lengths).~~

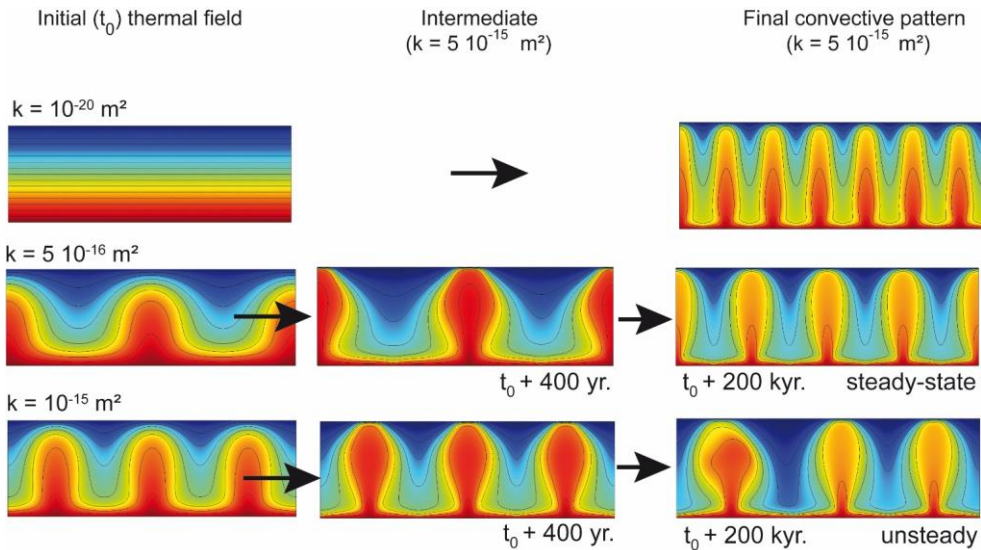


Figure 5. Illustration of “thermal inheritance”. For the three cases, the final permeability is the same but initial thermal regime differs ~~from one case to the other~~. In the first case (top row), ~~there is no thermal forcing since~~ the initial thermal regime is purely conductive (top left). A finger-like morphology is obtained for the upwellings. In the two other cases, the convective pattern appears to be controlled or influenced by the initial one. A bulb-like morphology is promoted for the upwellings. Color-bar (not shown) is the same as in previous figures.

Figure 6 shows similar experiments for different box lengths (5, 7 and 10 km): an instantaneous increase of the initial permeability k_0 is imposed. For each experiment, from (a) to (h), the initial thermal regime is on the top and the final pattern is below. Fig. 6a corresponds to the conditions of Fig. 1f, but box length has been slightly increased (5 km instead of 4.5 km). It follows that 7 internal finger-like upwellings are obtained (and not 6 as in Fig. 1f). For the same box length, the two other experiments (Fig. 6b and 6c) illustrate ~~the same phenomenon as previously described~~ (thermal inheritance): 3 internal upwellings are conserved in Fig. 6b and 4 upwellings in Fig. 6c. As in Fig. 3, the instantaneous permeability increase results in ~~the~~ shrinking of the upwelling tail (see white arrows), thus promoting bulb-like geometries. Without detailing the other experiments for box lengths of 7 and 10 km (Fig. 6d to 6h), it can be easily seen that thermal inheritance is a the rule. For each case, the final convective pattern appears to be controlled by the initial one (same number of upwellings).

Instantaneous increase of permeability: from k_0 to $5 \cdot 10^{-15} \text{ m}^2$

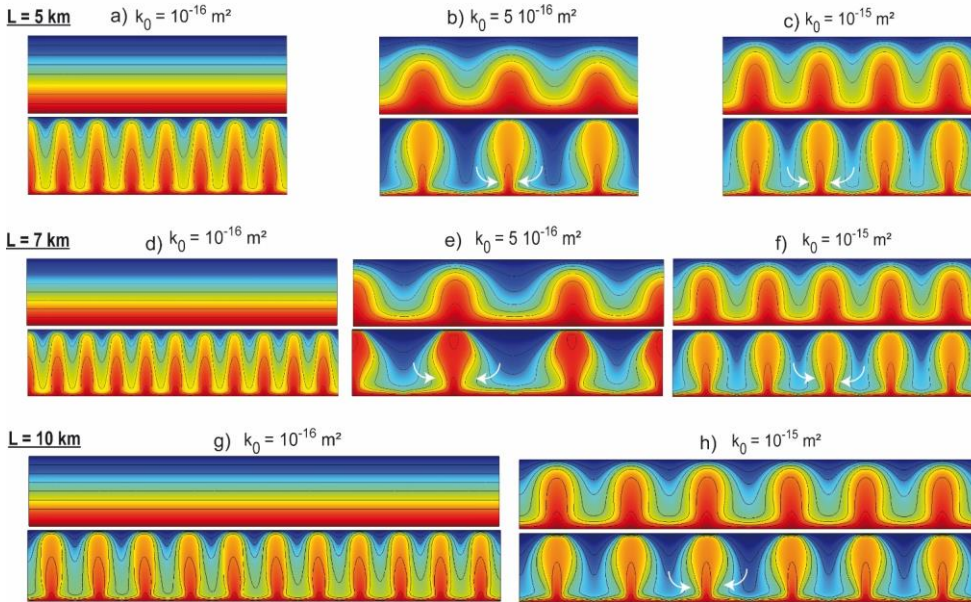
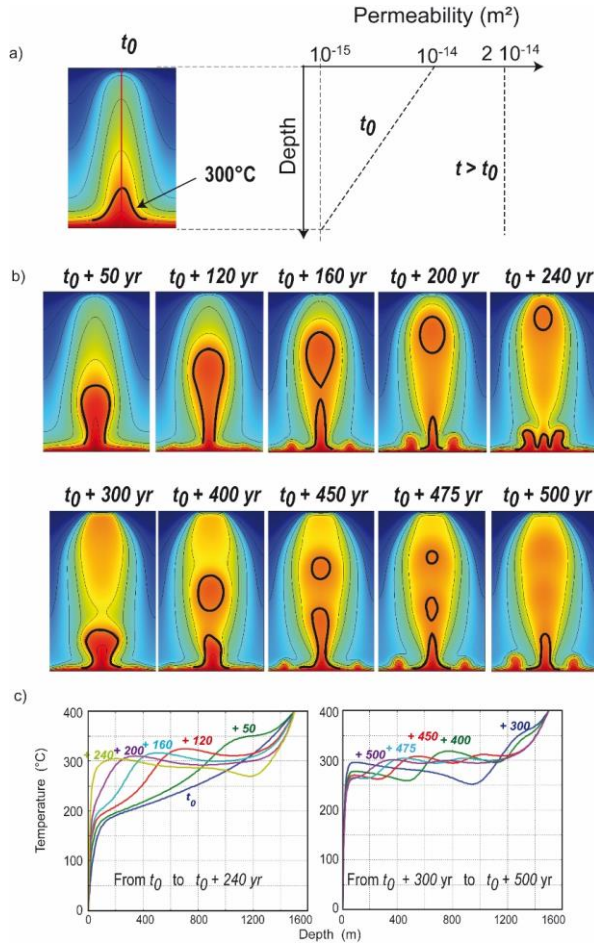


Figure 6. Additional experiments illustrating thermal inheritance for 3 distinct box lengths L . Initial ($t = t_0$) thermal regimes correspond to the figures on the top, obtained with the permeability k_0 . At $t > t_0$, for the 8 experiments, permeability is instantaneously increased from k_0 to $5 \cdot 10^{-15} \text{ m}^2$, and the obtained regime after a few hundreds of years is shown at bottom of each experiment. For each box length, the initial thermal regime can represent a conductive regime (cases a, d and g) or a slightly convective regimes (b, e) or a more vigorous convective regimes (c, f and h). For each case, the obtained convective pattern is strongly controlled by the initial one, i.e., the location of upwellings is dictated by that of the previous ones. Note that the finger-like shape of upwellings (a, d and g) is changed to a bulb-like shape with a shrinking base (white arrows) when the initial thermal regime is not conductive. Color-bar (not shown) is the same as in previous figures.

4.5 Case of high permeability: splitting-pulsating plumes

When permeability suddenly increases (Fig. 3 to 5), the bulb-like geometry is favored because hot buoyant fluid has less resistance to flow-upward flow, and fluid velocity increases. In the case of a high permeability involving fluid velocity greater than $\sim 10^{-7} \text{ m}\cdot\text{s}^{-1}$, the velocity increase involves the separation ofseparates the plume head from its tail, as already observed by Coumou et al. (2006) and Fontaine and Wilcock (2007), who observed "individual upflow zones". Figure 7 illustrates such a case, where initial permeability (depth-dependent permeability with a maximum value of 10^{-14} m^2) is increased to a constant value of $2 \cdot 10^{-14} \text{ m}^2$ (Fig. 7a). The initial convective pattern (triangular-like geometry) evolves promptly toward a bulb-like

525 geometry and a pulsating behavior is observed, exhibiting several splitting-individual stages of the hot upwelling. Even if this convective regime is probably close to a chaotic behaviour, one could however can define a time period of 240–250 yr in accordance with the results of Fontaine and Wilcock (2007). Indeed, Fig. 7 shows: that similar patterns are observed at time $t_0 + 50$ yr and $t_0 + 300$ yr, or at time $t_0 + 160$ yr and $t_0 + 400$ yr.



530 **Figure 7.** Instantaneous increase of the medium permeability (from $10^{-14} \exp(-z/650)$ at $t = t_0$, to $2 \cdot 10^{-14}$ m², at $t > t_0$) resulting in a high velocity upwelling, where the central blob does not lose much energy during ascent. a) steadySteady-state triangular-like

upwelling at $t = t_0$, and permeability function ; b) ~~temporal~~ Temporal evolution of the convective pattern showing the detachment of a high temperature « blob » ($T > 300^\circ\text{C}$); c) Plots of vertical temperature profiles taken at the blob vertical axis (red vertical line in the top left pattern) for each time step shown in b). Color-bar (not shown) is the same as in previous figures.

535 Starting from the initial stage, deep hot fluid accelerates and finally forms an isolated blob of fast hot fluid, separated from the tail. The black-contoured area in Fig. 7b contains fluid hotter than 300°C . Before the splitting-separation occurs, maximum fluid velocity reaches $3 \cdot 10^{-7} \text{ m}\cdot\text{s}^{-1}$ ($9 \text{ m}\cdot\text{yr}^{-1}$), whereas typical fluid velocity is around $5 \cdot 10^{-8} \text{ m}\cdot\text{s}^{-1}$ for a permeability of $5 \cdot 10^{-15} \text{ m}^2$ and around $10^{-8} \text{ m}\cdot\text{s}^{-1}$ for a permeability of 10^{-15} m^2 . Figure 7c illustrates the thermal signature of this ascending blob (or splitting-pulsating plume). It can be seen that vertical temperature profiles have ~~indeed~~ a locally negative temperature gradient
540 at $t_0 + 120 \text{ yr}$ and after. The multiple blobs illustrated at $t_0 + 450\text{--}475 \text{ yr}$ are also visible on labelled temperature profiles.

5. Results from 3D models

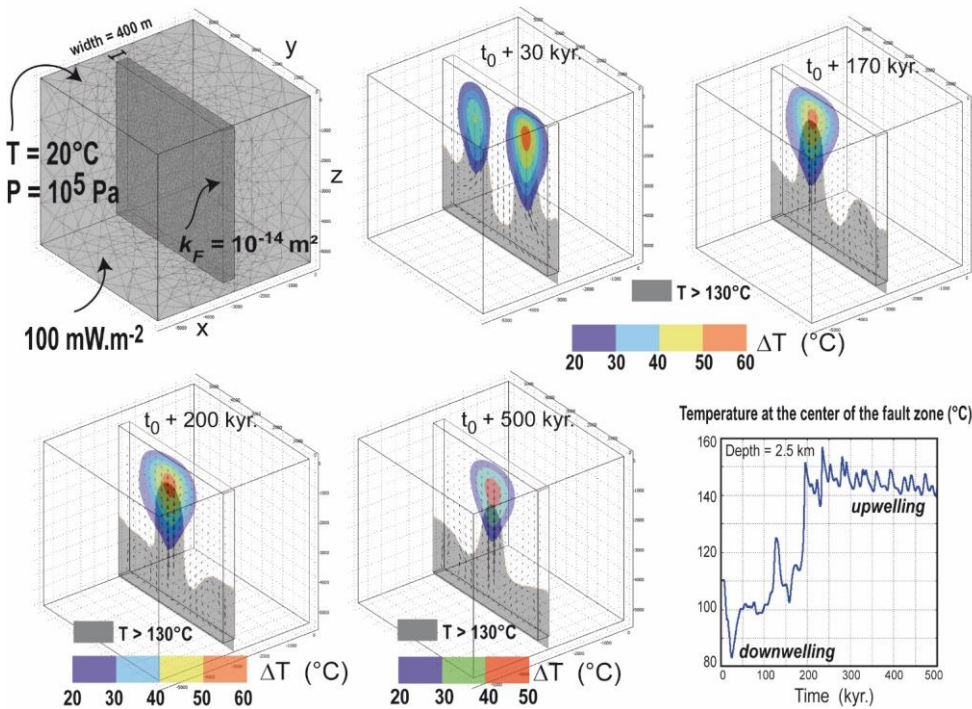
In the following, ~~the~~ simplified 3D numerical approach is focused on the case of a finite-size fault zone, embedded in a less permeable host rock. In order to validate our numerical approach and procedure, we first performed benchmark tests on the basis of a recently published study, where different teams worked on the same numerical scenario but with different finite
545 elements numerical codes, ~~say~~ OpenGeoSys, Golem and FEFLOW (Magri et al., 2017). As emphasized by the authors, despite similar convective patterns ~~were obtained~~, some quantitative differences in the results were observed, and interpreted as due to « discretization errors (spatial/temporal) » or different « solver settings ». Consequently, our benchmark test is also expected to reproduce qualitatively the same convective patterns ~~as those published by this study~~.

550 Benchmark tests and results are described in Appendix B. These tests consider a thin (40 m wide) fault zone with simplified fluid properties, identical to those of the Magri et al. (2017) study. In Appendix B, convective patterns, thermal and velocity fields, and temperature anomalies are detailed. The following experiments (below) are focused on the case of thicker permeable fault zones (100–400 m), where the fluid density law is more realistic than in the benchmark tests since it is temperature- and pressure-dependent (see Appendix A). The thermal boundary condition at the bottom of the box (depth 5500 m) is not 170°C
555 as in Magri et al. (2017) and in our benchmark experiment, but corresponds to a more realistic fixed heat flow condition of $100 \text{ mW}\cdot\text{m}^{-2}$, a typical value in favorable areas for geothermal exploration (e.g. Blackwell et al., 2006; Cloetingh et al., 2010; Erkan, 2015). However, for the problem geometries considered, this high basal heat flow will not induce temperature values higher than 210°C . To involve temperatures around $300\text{--}350^\circ\text{C}$, one would need to impose a basal heat flow condition around $180 \text{ mW}\cdot\text{m}^{-2}$, a value considered as too extreme for the purpose of this study (see however Della-Vedova et al. 2008, where
560 basal heat flow in Tuscany, Italy, would be around $150\text{--}200 \text{ mW}\cdot\text{m}^{-2}$). In the following, the role of a depth-dependent permeability and the effect of the fault dip angle are investigated. To avoid ~~discussing about~~ edge effects, the case of a longer fault is also presented.

5.1 Case of a vertical fault zone with a constant permeability

In the following experiment, which is derived from the benchmark case, the fault zone is 400 m wide, and 5 km deep, does not outcrop at the surface and does not reach the bottom of the box (depth 5.5 km). Its dip angle will be varied as well as its permeability value or variation. An averaged heat production of $2 \mu\text{W}\cdot\text{m}^{-3}$ is imposed in the entire model; to account for representative radiogenic heat production in a shallow granitic crust (Jaupart and Mareschal, 2011; Artemieva et al., 2017). Top left of Fig. 8 shows some of the boundary conditions, the missing others being no flow and no thermal exchanges.

5.5 km x 5.5 km x 5.5 km



570 Figure 8. Case of a wide vertical fault zone in a 3D block, with realistic fluid properties and boundary conditions. Fault permeability is fixed at 10^{-14} m^2 . Positive temperature anomalies above greater than 20°C are colored in the middle plane of the fault zone. Zones where temperature exceeds 130°C are shown in grey. Temperature evolution at the center of the fault zone illustrates the transition from a downwelling to an upwelling, from 150 to 200 kyr.

575 In Fig. 8, the fault permeability (k_f) is fixed at 10^{-14} m², while the host rock is supposed impervious ($k_H = 10^{-18}$ m²). The initial thermal regime for all the following 3D models corresponds to a purely conductive regime. Figure 8 illustrates the time evolution of positive temperature anomalies (colored zones, in the middle plane of the fault zone, defined as temperature excess when compared to the conductive case) together with the domain for which temperature is greater than 130°C (grey areas). Time evolution of temperature at a depth of 2.5 km within the fault zone is also shown.

580 Temperature anomalies in 3D exhibit ~~some kind of a~~ « hot air balloon morphology » (see one perpendicular view in the next Fig. 9), where the maximum value exceeds 50°C, for at least 200 kyr. ~~It must be emphasized that this~~ This same shape was ~~already~~ visible in the benchmark experiment (Appendix B, Fig. B1). This morphology could be ~~called assimilated to~~ the “geothermal reservoir”, whose size would be described by a given critical value of the temperature anomaly (e.g. $\Delta T > 30^\circ\text{C}$).

585 The absolute temperature value at a depth of 2.5 km also exceeds 150°C between 200 and 340 kyr (see temperature evolution in the lower right plot of Fig. 8). During the first 200 kyr., the convective pattern is mainly dominated by a central cold downwelling and two adjacent upwellings. With time, the pattern reverses for ~~promoting a~~ single hot central upwelling. This flow reversal was also observed for an inclined fault zone (see below).

5.2 Similar case for an inclined fault

590 Figure 9 shows an experiment where all parameters are identical to the previous one, except for the fault dip angle, here chosen at 30° from the vertical. Figure 9b illustrates the temperature field at $t_0 + 200$ kyr, at a depth of 2.1 km (colored plane), where a temperature of 150 °C is reached at the centre attained; it also shows the distorted 150°C isotherm (in red), ~~emphasizing~~ reflecting the upward fluid circulation, rising at a maximum velocity of $2.4 \cdot 10^{-8}$ m.s⁻¹ (0.75 m.yr⁻¹). Figure 9c illustrates the time evolution of temperature anomalies, from two « balloons » to a single one at times greater than $t_0 + 190$ kyr. During the transition from two to one single upwelling, the temperature anomaly decreases in amplitude, and then recovers values greater than 50°C (see time $t_0 + 215$ kyr). At the bottom left of Fig. 9c, a lateral view of the same temperature anomaly shows that (i) the temperature anomaly extends laterally to more than 500 m away from the fault zone boundaries; (ii) the maximum range of [50-60] °C extends ~~in from~~ a depth range of ~1.0 to 2.2 km. Figure 9d shows a downward temperature profile along the fault (A-B in Fig. 9a). The upward temperature anomaly is clearly visible and appears to be maximum at time $t_0 + 215$ kyr ~~(at~~

600 this time, a temperature of 150°C is reached at a depth of 1.5 km, as shown in Fig. 9b).

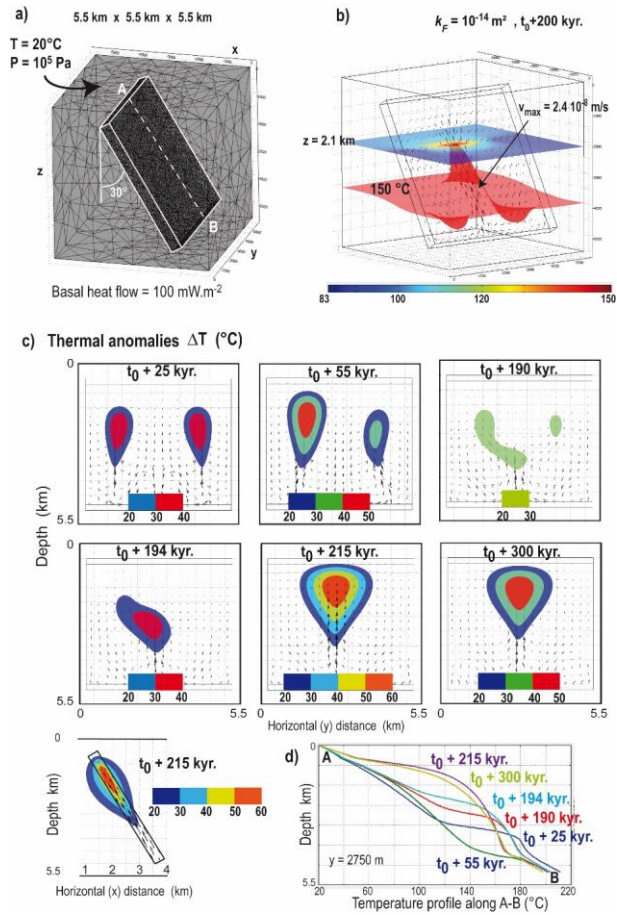


Figure 9. (a) Similar experiment as in Figure 8 but for an inclined (30°) fault zone. (b) a temperature of 150°C is reached at a depth of 2.1 km. Color bar corresponds to temperature values at a depth of 2.1 km; (c) temporal evolution of thermal anomalies (colored zones), viewed in a vertical plane: a similar transition from two upwellings to a single central one is observed. The other perpendicular view in the bottom left illustrates lateral diffusion of the anomaly within the host rock; (d) temperature evolution within the fault zone along the A-B profile.

5.3 Cases with a depth-dependent permeability

In the four experiments of Fig 10, a depth-dependent permeability (exponential decrease) is imposed within the fault, and the dip angle varies from 0 (vertical) to 45°. The maximum fault permeability ~~is here~~ is 20 times higher than in Fig. 8 and 9. For each dip angle, transient evolution of positive thermal anomalies are illustrated ~~with 3 time steps for which particular convective patterns have been selected.~~

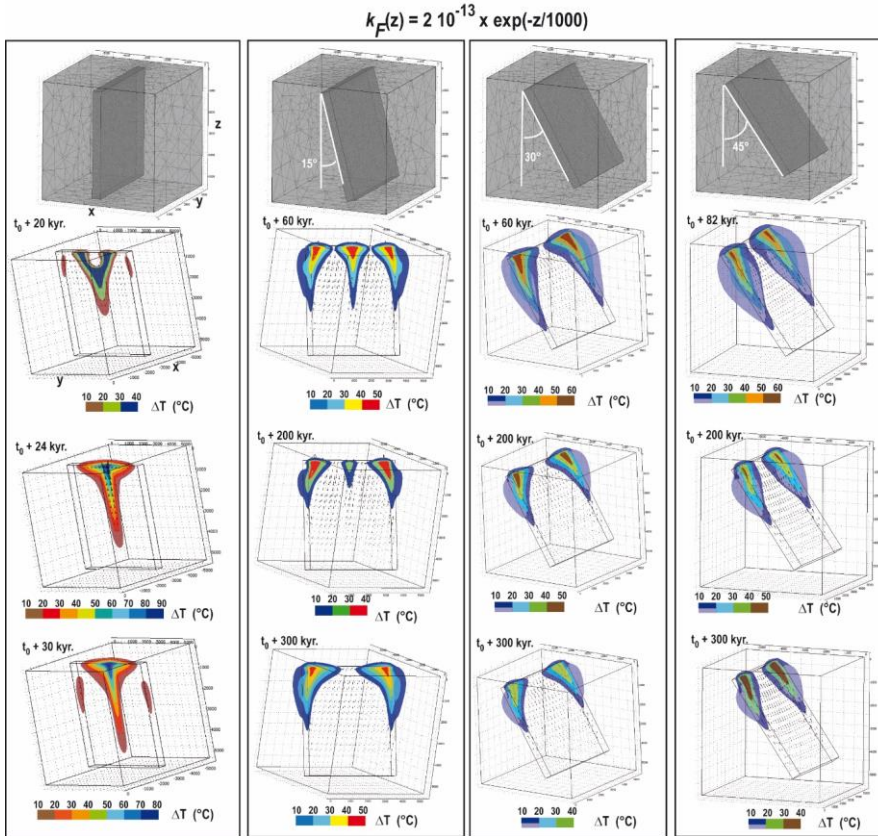


Figure 10. Four experiments with realistic fluid properties and a depth-dependent permeability, with a dip angle of 0, 15, 30 and 45°. Few differences exist between the two ~~last cases~~ higher dip angles. The largest temperature anomaly amplitudes are obtained in the vertical case (left) and during the first tens of kyr. In the second case (15° dip angle), a transient anomaly disappears after 200 kyr.

In the case of a vertical fault zone (left column), a quasi steady-state convective pattern is reached at time $t_0 + 24$ kyr. The initial anomaly exhibits a « Y-shaped » pattern ($t_0 + 20$ kyr) with a temperature anomaly lower than 40°C. With time, the Y-shaped anomaly evolves towards a « funnel-shape » pattern ($t_0 + 30$ kyr) with a much higher-value-for-the-larger temperature anomaly. Because permeability is higher at shallow depths, the anomaly ~~expends~~ expands laterally near the surface. From the top of the fault zone (at a depth of 500 m) to a depth of ~ 1.0 km, a temperature anomaly greater than 80°C (dark blue zone) and around 500 m wide, establishes. ~~If anomalies greater than 50°C are considered (from light to dark blue), then this distance is more than doubled.~~

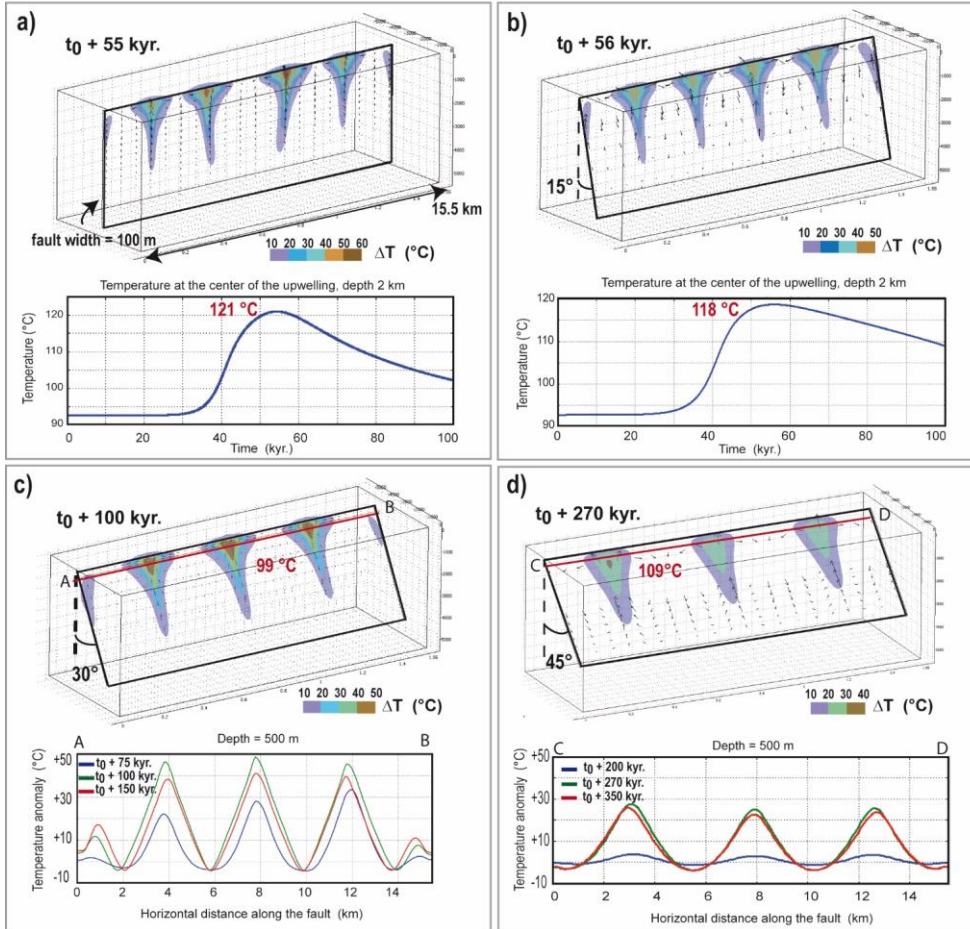
For the three other-cases dealing-with inclined fault zones (dip angles of 15, 30 and 45°), time evolution is much longer since quasi steady-state convective patterns ~~establish-are reached only~~ after 200 kyr. There are two main differences between these 3 experiments and the previous one (i.e. the vertical case). The first is that the number of anomalously warm upwellings ~~has been-increased~~ increases. At time $t_0 + 60$ kyr and for a dip angle of 15°, three anomalies (greater than 40°C) are identified. With time, the central one disappears ~~since-because~~ a central downwelling establishes, ~~thus~~ leaving two positive anomalies at fault edges. The second major difference ~~deals-with~~ is the value of temperature anomalies, which do not exceed 50-60°C in the case of an inclined fault zone, ~~whereas it exceeds 80°C in the vertical case~~. These results are consistent with the 2D models of Duwiquet et al. (2019), who also found higher thermal anomalies for vertical fault zones.

5.4 Case of a longer fault

The curved shape of lateral anomalies in Fig. 10 (for inclined fault zones) might be due to side-boundary effects since fault length is the same as fault height. The following experiments illustrate the case of a longer (15 km) fault zone, with a maximum permeability of $5 \cdot 10^{-13}$ m². In Fig. 11, fault width is reduced to 100 m and fault dip angle is varied. In Fig. 12, fault dip angle is fixed at 30° while fault width is varied from 100 to 400 m. Snapshots of experiments correspond to time steps during which thermal anomaly is maximum (see temporal evolution in Fig. 11a, and horizontal temperature profiles in Fig. 11b).

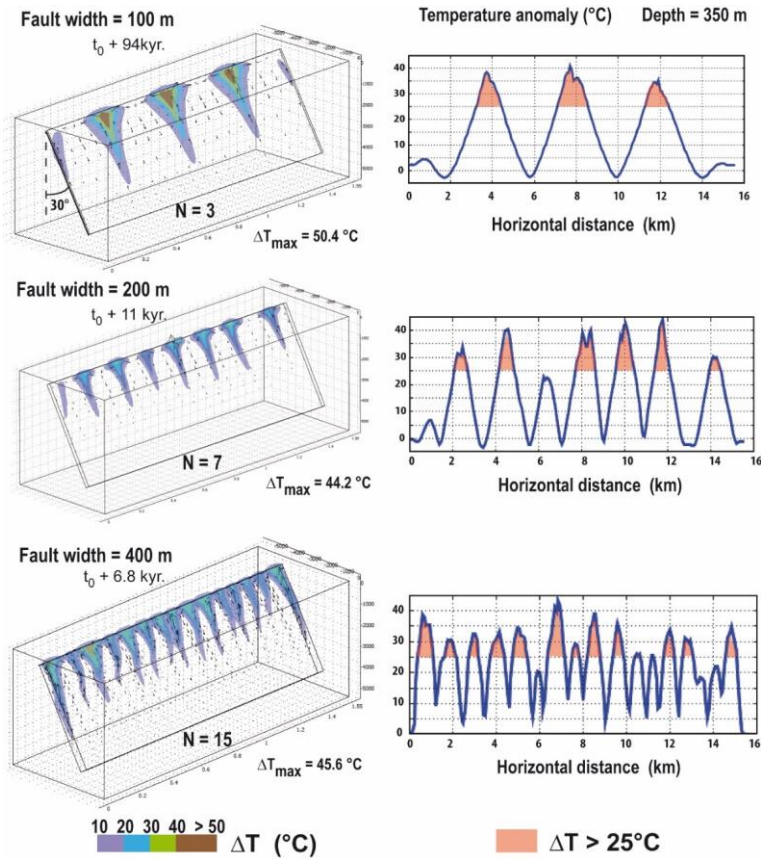
In all experiments, funnel-shaped thermal anomalies develop, ~~as-it-seems-to-be~~ controlled by the exponential decrease of fault zone permeability. Except for the vertical case (Fig. 11a), thermal anomalies do not exceed 50°C. The maximum temperature anomaly is reached more rapidly when fault dip angle is small (at $t_0 + 55$ kyr and $t_0 + 56$ kyr for 0 and 15°, respectively) or when fault width is large (at $t_0 + 6.8$ kyr for a 400 m wide fault). The two plots of temporal evolution in Fig. 11a show that the maximum temperature anomaly remains elevated (above 25°C) during ~ 20 kyr, a duration which could be regarded as representative of the lifetime of a geothermal system. Obviously, this value ~~must-be~~ is associated ~~to-with~~ the chosen permeability distribution.

$$k_F(z) = 5 \cdot 10^{-13} \exp(-z/1000)$$



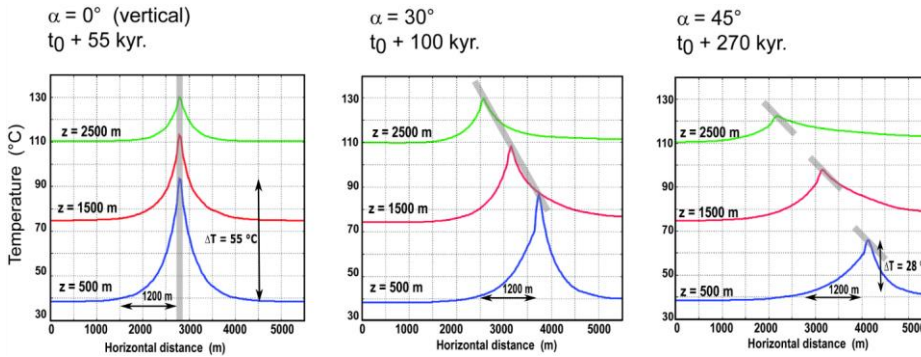
650 Figure 11. Experiments with a longer (15.5 km long) fault, with different dip angles (0, 15, 30 and 45°). Permeability is depth-dependent with a maximum value of $5 \cdot 10^{-13} \text{ m}^2$ for each case. The obtained temperature anomalies slightly exceed 50°C in the vertical case only. Each time step Cross sections illustrates the maximum temperature anomaly obtained during the entire experiment. Time evolution of temperature (top) or temperature anomalies (bottom) are shown beneath temperature anomaly patterns.

655 Figure 12 shows that the wider the fault, the higher is the number of funnel-shaped anomalies. This results in an almost continuous thermal anomaly at shallow depth (see horizontal profiles at a depth of 350 m, right column of Fig. 12). Figure 13 illustrates thermal diffusion in host rocks: the anomalously high temperatures extend over a distance of 2.4 km (1200 m for each side). Fig. 13 also illustrates that a vertical fault zone (left case) induces a much higher temperature anomaly (64°C at a depth of 500 m) than an inclined fault zone (only 38°C on the right case), as already so observed in Fig. 10 and 11.



660

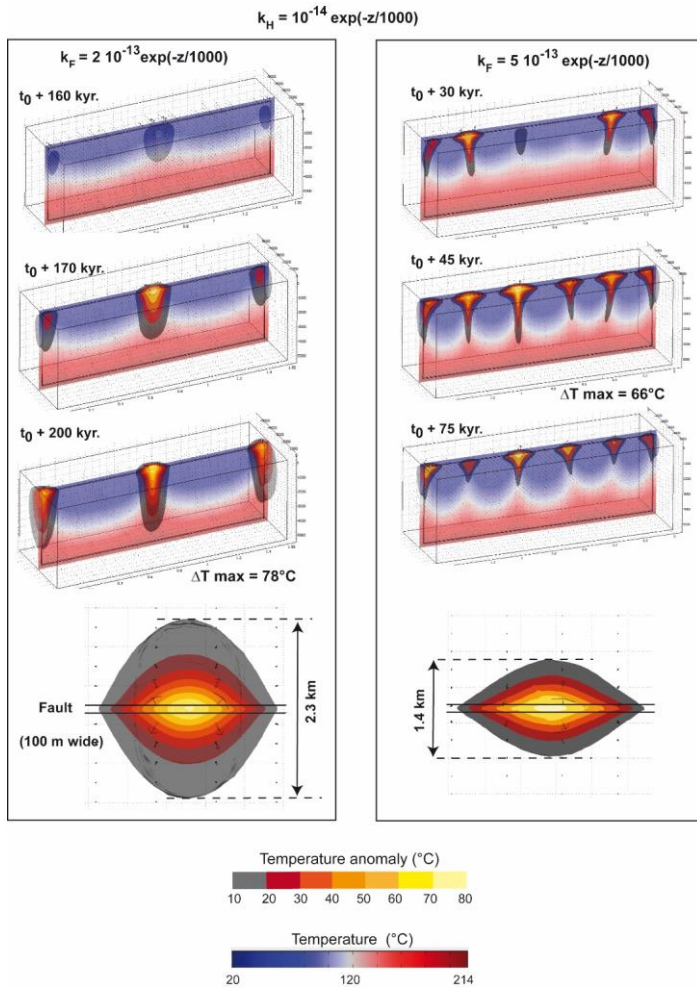
Figure 12. Effect of fault width on temperature anomaly pattern for the same dip angle of 30° and the same permeability law as in Fig. 11. Values of maximal temperature anomalies are similar, but the wider the fault, the more numerous are the positive thermal anomalies. Temperature anomalies greater than 25°C at a depth of 350 m are illustrated highlighted on the right of each case.



665 Figure 13. Effect of fault dip angle (the angle is illustrated by grey rectangles) on horizontal profiles of temperature, perpendicular to the fault zone, at the time when temperature anomaly is maximum (indicated on top of each case). While the lateral diffusion length remains similar (~1200 m on each side, at a depth of 500 m, and ~800-900 m at a depth of 2500 m), the amplitude is clearly greater in the vertical case (~55°C at a depth of 500 m in the vertical case, and ~28°C for a dip angle of 45°).

670 To this point, all of our numerical experiments have assumed the host rock to be impermeable. Here we consider some of the effects of permeable host rock. Finally, Figure 14 shows temporal evolution of thermal anomalies superimposed on the temperature field within a 100 m wide vertical fault zone. Two different permeability fields in the fault zone are illustrated, so that and the ratio between fault permeability and host rocks permeability equals 20 and 50. While only one internal upwelling dominates in the left-low-ratio case, four upwellings are obtained in the case of the most-more permeable fault zone. Because fluid velocity is smaller in the first-low-ratio case (the maximum temperature anomaly is reached at $t_0 + 200$ kyr, but only at versus $t_0 + 45$ kyr in the permeable case), thermal diffusion and heat advection into the host rocks occurs into a wider volume is more effective (compare the two horizontal map view at the bottom of Fig. 14). Although the along-fault dimension of the two thermal anomalies are similar (2.3 and 2.5 km) their width differs by almost a factor of 2. Another important difference deal with the amplitude of the The maximum temperature anomaly: while it reaches 78°C in the left-low-ratio case, it only reaches and 66°C in the permeable case. Consequently, from these two experiments, one could conclude that the volume and the potential of the “geothermal reservoir” appears more important are greater for the smaller permeability ratio, which would favor higher temperatures and wider thermal diffusion, but additional experiments with higher permeability ratios, as in Duwiquet et al. (2019) are required. Actually, one One last experiment, not shown here, and with an because the imposed basal heat flow was $150 \text{ mW} \cdot \text{m}^{-2}$, was carried out with a permeability ratio of 100. Three funnel-shape anomalies developed, with a maximum amplitude of 120°C centered at 500 m depth. For this particular experiment, temperatures of 150°C were reached at a depth of 750 m. Temperature anomalies exceeded 70°C over a depth range of 3 km and a lateral dimension of 700 m.

685



690 | Figure 14. Effect of permeability ratio between the vertical fault zone and the host rocks: $k_F/k_H = 20$ (left) and 50 (right). Maximum temperature anomaly is reached at time $t_0 + 200$ kyr (left) and $t_0 + 45$ kyr (right). Bottom figures show temperature anomalies from above at a depth of 500 m. While the maximum amplitudes of the anomalies do not differ much (66 and 78°C), the lateral diffusion lengths strongly differ (2.3 and 1.4 km wide).

6 Discussion

695 The main objective of this study ~~consisted in~~ ~~was to investigating~~ ~~investigate~~ the various possible convective patterns and the associated thermal anomalies in a permeable fault zone. ~~The~~ 2D experiments were first performed to validate our numerical approach by reproducing the published results ~~by of~~ Rabinowicz et al. (1998), and can be viewed as fluid circulation models along a fault plane, without accounting for ~~the embeddings~~ ~~mass exchanges with the host rock~~. Some particular processes ~~have been underlined~~ ~~were highlighted~~ (such as the thermal inheritance mechanism) and are ~~further~~ discussed below. When more realistic fault zones are considered, i.e. when damage zones of several tens to hundreds of meters are taken into account, 3D
700 experiments are required, since convective patterns are expected to also depend on host rock properties. In ~~the~~ 2D experiments, boundary conditions and fluid properties were chosen to reproduce the results by Rabinowicz et al. (1998) and ~~the~~ fluid density law ~~was~~ in particular ~~was~~ simplified (Appendix A). In ~~the~~ 3D experiments, more realistic physical conditions are applied: fluid density is temperature- and pressure-dependent, and the bottom thermal boundary condition corresponds to a fixed heat flow of 100 mW.m⁻². ~~Our approach differs from the “discrete fracture flow” approach where fracture networks consist in discrete~~
705 ~~thin fault planes (e.g. Mezon et al., 2018). Here, the fracture flow approach is not appropriate because thickness of crustal fault zones may exceeds hundreds of meters.~~

6.1 2D convective patterns

In the first series of 2D models, the well-known finger-like convective pattern was reproduced for a constant permeability (Fig. 1). Because of lithostatic pressure, permeability ~~generally~~ decreases with depth, and the use of a more realistic
710 permeability distribution appears to change the finger-like pattern towards a triangular-like pattern (Fig. 2) with a dominant cooling effect. Indeed, the most permeable levels being at shallow depths, cold downwellings are favored. This may explain why, along permeable fault zones, hot upwellings (evidenced by emergence of thermal springs) are not numerous and irregularly spaced.

715 ~~Actually, E~~quivalent effects ~~are obtained in~~ ~~might be caused by~~ presence of ~~significant~~ ~~an important~~ topography (> 1500 m), ~~causing since~~ infiltrating cold fluids ~~to at high altitude~~ dominate and prevent hot fluids ~~to rise at~~ ~~from rising to~~ the surface, except in a few locations (see the clusters of thermal springs in the Pyrenees, in Taillefer et al., 2017). The role of topography on the location ~~of clusters~~ of thermal springs in the Jordan rift valley has also been investigated by Magri et al. (2015), who illustrated the ~~possible~~ coexistence of topography-driven ~~flow~~ and buoyancy-driven flow. ~~Consequently, our results should~~
720 ~~not be considered as soon as topography is important since topography~~ ~~Topography~~-driven flow ~~may can~~ predominate and modify the convective patterns. Nevertheless, the results shown in Fig. 2 indicate that when topography is not important, ~~the~~ depth-dependent permeability may have similar consequences ~~as a significant topography~~.

In Fig-~~ures~~ 3 and 4, ~~the~~ instantaneous and continuous increases of permeability modify the initial convective pattern (triangular-like or finger-like) to form bulb-like convective patterns, with a significant temperature increase at shallow depth. Conversely, ~~the a~~ decrease in permeability ~~allows recoveringrecovers~~ the finger-like pattern, accompanied by ~~a~~ short-duration cooling ~~event~~ (Fig. 4). This process might be of major importance for geothermal exploration around active fault zones, where permeability is probably at its maximum. In other words, active fault zones could host geothermal reservoirs with a kilometer-scale bulb-like geometry (see also Patterson et al., 2018a; Wanner et al., 2019).

The thermal inheritance concept illustrated in Fig. 5 and 6 may be relevant for a number of geological processes involving circulation of deep hot fluids. Studies on gold metallogeny (orogenic gold deposits, ~~BIF-hosted~~ gold deposits ~~in banded iron formations, gold in volcanic massive sulfides~~) have often suggested polyphased mineralizing events (e.g. Bonnemaison and Marcoux, 1990; ~~Coumou et al., 2009~~; Lawley et al., 2015; Gourcerol et al., 2020). This mechanism could indeed be at the origin of polyphased hydrothermal ore deposits in the sense that a structure already mineralized could be more favourable for focussing the latter hydrothermal stages. ~~It must be noted that while~~While “structural inheritance” ~~was has been~~ invoked many times to explain strain localization or tectonic history of mountain belts (e.g. Jammes et al., 2013), thermal inheritance appears as another physical mechanism that may play an important role in the wide range of thermo-mechanical processes.

Finally, the ~~splitting-pulsating~~ behavior observed in Fig. 7 has been used by Deveaud et al. (2015) to suggest one possible dynamical mechanism at the origin of rare-elements pegmatite emplacement. Indeed, these ~~fluent-rich~~ magmatic liquids have an extremely low viscosity (e.g. Bartels et al., 2013). Consequently, the associated dynamic permeability (the ratio between static permeability and fluid viscosity) is anomalously high, and ~~their~~ escape and detachment from a deep crustal magma source through permeable shear zones is facilitated. Successive separations from a magma source could ~~represent an alternative process to~~ explain the differences in chemical enrichment within a single pegmatite field (Melleton et al., 2015). ~~In addition, the splitting behaviour may represent one way to expulse hot blobs of magma that would crystallize away from their source, a mechanism which could help resolving the “pegmatite paradox” (Butler and Torvela, 2018). In addition to thermal inheritance, this~~The pulsating behaviour observed in Fig. 7 was also suggested by Link et al. (2019) to ~~help~~ explain the multiphase gold mineralizing events in fault zones of the Pyrenees, south of France.

6.2 3D hydrothermal convection and temperature anomalies

The understanding of 3D hydrothermal convection in fault zones ~~made some important~~has progressed in the last decades. Recently, a new Rayleigh number expression based on fault geometry and on physical fluid and rock properties has ~~been~~ proved to be ~~more better~~ adapted than the Rayleigh theory to define the onset of thermal convection (Malkovskii and Magri, 2016). ~~As far as n~~Numerical modeling of 3D hydrothermal convection ~~is concerned, has considered~~ numerous geological examples ~~have been studied~~, from the fractured oceanic lithosphere to fault zones (e.g. Rabinowicz et al., 1998; Fontaine et

al., 2001; Zhao et al., 2003; Bächler et al., 2003; Kuhn et al., 2006; Baietto et al., 2008; Harcouët-Menou et al., 2009; Coumou et al., 2009; McLellan et al., 2010; Person et al., 2012; Andersen et al., 2015; Magri et al., 2016; Malkovski and Magri, 2016; Magri et al., 2017; Taillefer et al., 2018; Patterson et al., 2018a; Patterson et al., 2018b; Bauer et al., 2019). For each case, some surprising dynamical features were discovered, ~~like such as~~ the thermal interference between separated fractures (Patterson et al., 2018b), or the helicoidal fluid flow pathways (Magri et al., 2016). However, the anomalously high temperatures at shallow depths were not necessarily studied in detail.

Patterson et al. (2018a) have reproduced typical convective patterns such as those described in our 3D benchmark tests (Fig. B1), but for thinner fractures (up to 10 m wide) of elliptical geometry. The values of their obtained temperature anomalies (see their Fig. 3) are ~~at least twice lower much smaller~~ (not greater than $\pm 15^\circ\text{C}$) than those obtained in our benchmark tests, where fault width equals 40 m. However, geometry of their thermal anomalies ~~remains was~~ similar and shows a “hot air balloon” morphology. Person et al. (2012) illustrated the role of fault intersections on temperature anomalies at the surface, for fault permeability values ranging from 2 to $7 \cdot 10^{-13} \text{ m}^2$. Transient evolution shows that temperature anomalies up to 92°C can be achieved. Yet, in their experiments, fault widths are small (10 and 20 m), ~~but and~~ a « spring » thermal boundary condition (no vertical temperature gradient) was imposed at the surface, in the lowlands of their model, ~~including spanning~~ the vertical fault zones. This boundary condition ~~should probably may~~ favor upflow of deep hot fluids within these highly permeable structures and their temperatures anomalies might be overestimated. Our 3D models show that, without imposing a spring condition at the surface, temperature anomaly up to 90°C may indeed ~~settle occur~~ at the top of a non-outcropping vertical fault zone (Figure 10, vertical case).

According to previous studies where width of the fault zone is smaller than 100 m, and ~~with considering also~~ our results where widths exceed 100 m, it seems that the wider the fault, the ~~higher is larger~~ the temperature anomaly: around 30°C for a 40 m wide fault zone (Appendix B); around $50\text{--}60^\circ\text{C}$ when fault width equals or exceeds 100 m, (e.g. Fig. 11) and up to $80\text{--}90^\circ\text{C}$ when the fault zone is wide and vertical (Fig. 10, left and Fig. 14). Nevertheless, this is not the case ~~for the dipping fault~~ in Fig. 12, where only fault zone width varies, from 100 to 400 m, and ~~where temperature anomaly remains~~ around $50 \pm 10^\circ\text{C}$. ~~Actually, T~~ the most important parameter could be the fault dip angle, as illustrated in Fig. 10, and as ~~already~~ suggested by Ahtziger-Zupančič et al. (2016). However, permeability distribution plays clearly a role, and it is probably the combination ~~between of~~ fault width, fault permeability distribution and dip angle which controls the ~~amount movement~~ of energy towards the surface (e.g. Roche et al., 2019). A more systematic study on all these parameters should allow ~~to build the construction of~~ a regime diagram for 3D convective patterns.

6.3 Morphology of thermal anomalies

~~The amount of energy has been recently illustrated by~~ Wanner et al. (2019) ~~who~~ modelled the effect of a vertical upflow in a permeable (10^{-13} m²) zone (area of 150 m × 100 m). They obtained an ellipsoidal vertical thermal plume providing 120°C at a depth of 2 km. Morphology of their thermal anomaly is close to our “hot air balloon” morphologies (Fig. 8 an 9), although boundary conditions differ: in their model, an overpressure is imposed at the base of the upflow zone, and a fixed temperature of 4°C is imposed on the top surface, preventing any lateral expansion of the anomaly (our funnel-shaped anomalies). The fact that we obtained a temperature of 150°C at a depth of 2.1 km w (Fig. 9b., where fault zone permeability is 10^{-14} m²) may be due to buoyancy-driven flow, which does not appear to play a role in the Wanner et al. (2019) study. This difference may also be due to the different boundary conditions and initial thermal regimes. Nonetheless, ~~the a similar~~ lateral thermal diffusion of the anomaly is obtained in both cases, thus defining the lateral dimension (2-4 km) of a geothermal reservoir.

The “hot air balloon” morphology can also be seen in the Patterson et al. (2018a) study where temperature perturbations vary according to the imposed fault permeability. It can be seen in their Fig. 3 that thermal diffusion ~~in-to~~ the host rocks results in anomalies of quasi-circular shape, similar to what is shown in Appendix B (Fig. B2b). In our experiments, the “hot air balloon” morphology was not the unique shape. Indeed, the “funnel-shape” anomalies illustrated for instance in Fig. 10, 11, 12 and 14, seem to dominate as soon as fault permeability is depth-dependent and convection sufficiently vigorous. As already mentioned, it is difficult to use the Rayleigh number theory to define the “vigor” of the convection, but clearly, one can see that convective patterns are more and more disturbed when fault permeability increases, when fault width increases and when fault dip angle is close to zero. As an example, the quasi-circular shape obtained in map view (e.g. Fig. B2b, but also in Fig. 14, bottom left), becomes more ovoid when permeability ratio between the fault zone and the host rocks is increased. Indeed, in that case, fluid velocity being higher, the host rocks are less imprinted by the hot rising fluid, and diffusion of the thermal anomaly extends over a smaller distance (bottom right of Fig. 14). This process may have important consequences on geothermal exploration since the interesting volume where thermal anomalies could be exploited (the geothermal reservoir) may strongly depend on permeability ratio.

6.4 Permeability ratio

As ~~already~~ mentioned by several ~~previous~~ studies, and observed here again, temperature is not necessarily ~~the-an~~ adequate parameter to describe hydrothermal convection (Fig. 1) and to define which convective regime will dominate. ~~According to Börsing et al. (2017) and Niederau et al. (2019), enthalpy or entropy production could be more appropriate.~~ Indeed, Fig. 1 (2D models) as well as Fig. 14 (3D models) illustrate that temperature values do not necessarily increase regularly when permeability increases. As pointed out by several authors (e.g. Lopez and Smith, 1995 ; Baietto et al., 2008), permeability ~~of the embeddings~~ heterogeneity is also important. In a recent compilation of measured or inferred permeability values in fault

820 zones, Scibek (2020) indicates, when available, the permeability ratio between the fault zone and ~~the-its~~
~~embeddings-surroundings~~. Duwiquet et al. (2019) suggested a regime diagram for different 2D convective patterns as a function
of permeability ratios. However, permeability ratio is probably also depth-dependent. In Fig. 14, the same depth-decrease of
permeability has been chosen ~~for the fault zone and its surroundings~~, so that a permeability ratio of 20 and 50 can be defined,
but it may not be representative of real fault zones, where the depth-decrease is probably more important in the surrounding
825 rocks. The question ~~of~~ whether fault zone permeability remains elevated at depth is crucial, since it may ~~involve-control~~
upwellings of deep hot fluids ~~at-to~~ shallow depths. According to Achtziger-Putančič et al. (2017), that might be the case for
dense networks of overlapping fault damage zones.

6.5 Amplitude and diffusion of thermal anomalies

As shown in Fig. 14, the horizontal cross sections of the anomaly may differ ~~for-two-for~~ different ~~fault zone / host rock~~
830 permeability ratios. Indeed, the ~~fastest-faster~~ the fluid can rise, the shorter is the time ~~period-during-which~~for thermal diffusion
~~occurs-within~~into the host rock. ~~However-it-is-important, however, to note that~~ the maximum amplitude of the anomaly is
similar in both cases of Fig. 14 (78 and 66°C). Hence, for these ~~2~~ experiments, permeability ratio does not seem to play a
significant role on the amplitude of the anomaly. ~~On-the-opposite, Fig-ure~~ 13 shows that fault dip angle seems to control the
835 amplitude of the anomaly: at the depth of 500_m (blue curves), the amplitude reaches 55°C for the vertical case (left) and then
decreases down to 28°C for a dip angle of 45°C. ~~On-the-other-hand, the~~The thermal diffusion length remains the same for the
three cases (~ 1200 m at a depth of 500 m). This length scale is in line with the results of lateral heating deduced by Wü
stefeld
et al. (2017), and with spatial distribution of paleotemperature estimates measured on carbonaceous material by Link et al. (2019)
across an auriferous shear zone.

6.6 Limits and perspectives

840 These preliminary 3D experiments of hydrothermal convection in fault zones, based on a successful benchmark test, have been
simplified (no topography, ~~simple fault zone~~ geometry ~~of-the-fault zone~~, homogeneous host rocks, no time-dependence of
permeability, fluid properties of pure water) in order to investigate the role of a few parameters on convective processes. As
emphasized by many authors (e.g. Ingebritsen and Appold, 2012; Ague, 2014), hydrothermal convection is complex, and the
fact that we account for the fault dip angle in addition to the 3D geometry and the depth-dependent permeability was considered
845 as a sufficiently elaborate model. Clearly, it would be worth ~~while~~ to perform 3D experiments related to real-~~case~~ studies
including surface topography, fault intersections and other key geological ~~features-being-prone-to-disturb-the-convective~~
~~patterns-identified-in-this-study~~. When such ~~kind-of~~ approaches ~~were-have-been-undertaken~~performed, one objective was to
reproduce – for instance – the location and temperature of thermal springs, or temperature and heat flow data (e.g. Magri
et al., 2015; Magri et al., 2016; Taillefer et al., 2019; Roche et al., 2018; Duwiquet et al., 2019). This is not the case ~~of-for-our~~
850 study which is ~~conceptual-in-nature-and~~ focused on the physical processes leading to the establishment of thermal anomalies
at shallow depths.

The first 2D ~~fault zone~~ models reproduced ~~mechanisms involving~~ high temperatures ($> 300\text{ }^{\circ}\text{C}$) since they were based on benchmark tests resulting from models of hydrothermal convection in oceanic ridges (Rabinowicz et al., 1998). For 3D models of fault zones, a more realistic basal heat flow of $100\text{ mW}\cdot\text{m}^{-2}$ was assumed, but temperatures did not exceed 214°C . Further modelling may have to consider deeper systems (e.g. crustal fault zones reaching at least a depth of 10 km) involving temperatures that would be present around the brittle-ductile transition.

Another ~~next~~ step for further 3D models should account for dynamic (time-dependent) permeability, since transient unexpected changes in the convective patterns were obtained in the 2D models with dynamic permeability (e.g. Fig. 3 and 4). For example, one may observe transitions from “hot air balloon” morphology in the case of a low permeability, to funnel-shape patterns after a sudden permeability increase. ~~In addition, only~~ 2 permeability ratios were investigated (Fig. 14), whereas many authors demonstrated that ~~it represents at this~~ major parameter being able to modify discharge temperatures and local heat flux (e.g. López and Smith, 1995; Baietto et al. 2008; Duwiquet et al., 2019). It is ~~thus~~ probable that different morphologies (not only funnel-shaped) could appear when permeability ratio is varied over a wider range.

Finally, it is well known that fluid composition (especially its salinity) strongly affects the density variation with temperature and pressure (Weis et al., 2014). ~~Our simplified choice of using pure water density law consists in giving a starting frame for investigating possible morphologies of thermal anomalies, but~~ a more realistic density law should be incorporated in future studies. ~~Consequently, our~~ Our results can probably be applied to crustal fault zones away from strong topography and ~~which are~~ not related to an underlying magmatic system (non-magmatic geothermal systems, Moeck, 2014).

7 Conclusion

The aim of this work was to investigate the ~~respective~~ role of different selected parameters on the shape and locations of thermal anomalies induced by hydrothermal convection in permeable fault zones. Through idealized and simplified 2D and 3D numerical models, a series of different convective patterns were obtained, depending mainly on (i) spatial and temporal variations of permeability and (ii) fault zone thickness and dip angle. Some new thermal processes identified in 2D (thermal inheritance, splitting-pulsating plumes ~~with a pulsating behaviour~~) were not tested in 3D but should clearly represent the research objectives of further 3D modelling studies. ~~Nevertheless, our~~ Our preliminary 3D results have shown that thermal anomalies, either of “funnel” shape or of “hot air ballon” morphology, can easily exceed 50°C over a depth range of one kilometer. In the case of vertical fault zones, temperature anomalies may reach $80\text{-}90^{\circ}\text{C}$, and those anomalies greater than 30°C can extend laterally ~~over~~ more than 1 km from the fault boundary.

885 Although it was not possible to isolate a single controlling parameter, it appears that the amplitude of positive thermal anomalies is ~~more important-greatest~~ when the fault zone is vertical. If one exploration guide ~~would have~~ were to be defined from these preliminary results, ~~it is that~~ one would clearly opt for the vertical fault zones. However, fluid velocity in vertical fault zones may be so high that thermal diffusion would have no time to heat significantly the surrounding rocks. A subtle balance between permeability of the fault zone and that of ~~the embeddingsits surroundings~~, may result in a large volume of anomalously hot rocks, thus creating interesting targets for geothermal exploration.

890

Appendices

Appendix A: Governing equations, fluid and rock properties and numerical procedure

In this study, numerical simulations of hydrothermal convection have been performed with the Comsol Multiphysics™ software (finite element method), by coupling Darcy law, heat equation and mass conservation. Details on these equations can be found in Guillou-Frottier et al. (2013). Three different fluid and rock properties have been used in the simulations. First, for 2D experiments, same fluid and rock properties as in Rabinowicz et al. (1998) have been chosen in order to reproduce some of their results (Figure 1d and 1f). For example, the fluid density law for these 2D experiments is:

$$\rho_L(T) = 1036.5 - 1416.7 \cdot 10^{-4} \times T - 2238.1 \cdot 10^{-6} \times T^2 \quad (\text{A1})$$

where subscript L means liquid, where density ρ_L is in $\text{kg}\cdot\text{m}^{-3}$, and temperature T is in $^\circ\text{C}$.

Second, for 3D benchmark experiments (see Appendix B), which refer to published results by Magri et al. (2017), same physical properties have been chosen. In particular, the density law varies linearly with temperature and is written, in the 0-150 $^\circ\text{C}$ domain:

$$\rho_L(T) = 1022.38 \times (1 - 0.00059 \times (T - 20)) \quad (\text{A2})$$

where T is in $^\circ\text{C}$.

Third, for the other 3D experiments (Fig. 8 to 14), more realistic fluid and rock properties have been used. Indeed, fluid density law is not only temperature-dependent but also pressure-dependent. The chosen fluid density law corresponds to a polynomial function, fitting experimental data for pure water and for temperature and pressure ranges of 0–1000 $^\circ\text{C}$ and 0–500 MPa (NIST Chemistry Webbook, Linstrom and Mallard, 2001; Launay, 2018):-

$$\begin{aligned} \rho_L(T,P) = & 1006 + (7.424 \cdot 10^{-7} \times P) + (-0.3922 \times T) + (-4.441 \cdot 10^{-15} \times P^2) + (4.547 \cdot 10^{-9} \times P \times T) \\ & + (-0.003774 \times T^2) + (1.451 \cdot 10^{-23} \times P^3) + (-1.793 \cdot 10^{-17} \times P^2 \times T) + (7.485 \cdot 10^{-12} \times P \times T^2) \\ & + (2.955 \cdot 10^{-6} \times T^3) + (-1.463 \cdot 10^{-32} \times P^4) + (1.361 \cdot 10^{-26} \times P^3 \times T) + (4.018 \cdot 10^{-21} \times P^2 \times T^2) \\ & + 7.372 \cdot 10^{-15} \times P \times T^3 + (5.698 \cdot 10^{-11} \times T^4) \\ & 1006 + (7.424 \times T) + (-0.3922 \times P) + (-4.441 \cdot 10^{-15} \times T^2) + (4.547 \cdot 10^{-9} \times T \times P) + (-0.003774 \times P^2) + \\ & (-1.451 \cdot 10^{-23} \times T^3) + (-1.793 \cdot 10^{-17} \times T^2 \times P) + (2.955 \cdot 10^{-6} \times P^3) + (-1.463 \cdot 10^{-32} \times T^4) + (-1.361 \cdot 10^{-26} \times \\ & T^3 \times P) + (4.018 \cdot 10^{-21} \times T^2 \times P^2) + (-7.372 \cdot 10^{-15} \times T \times P^3) + (5.698 \cdot 10^{-11} \times P^4) \end{aligned} \quad (\text{A3})$$

Mis en forme : Police :Times New Roman, Non Italique

where temperature T is in °C and pressure P in Pa. The fluid viscosity is only temperature-dependent and follows the exponential decrease as given in Rabinowicz et al. (1998):

$$\mu(T) = 2.414 \cdot 10^{-5} \times 10^{\frac{247.8}{(T+133)}} \quad (\text{A4})$$

where viscosity μ is in Pa.s and T in °C. All other properties of the fluid are identical as those used in many studies: heat capacity $C_{pL} = 4180 \text{ J.kg}^{-1}.\text{K}^{-1}$, thermal conductivity of the liquid $k_L = 0.6 \text{ W.m}^{-1}.\text{K}^{-1}$. Host rock properties are also typical for granitic rocks: density of the solid (S) $\rho_S = 2700 \text{ kg.m}^{-3}$, heat capacity $C_{pS} = 800 \text{ J.kg}^{-1}.\text{K}^{-1}$, thermal conductivity $k_S = 3.0 \text{ W.m}^{-1}.\text{K}^{-1}$, heat production rate $A = 2 \mu\text{W.m}^{-3}$. It must be pointed out that absolute values of these physical properties are not critical since permeability values can vary by several orders of magnitude and thus largely control the regime of hydrothermal convection.

Porosity in the host rock is taken at 1% while it amounts to 20% in the fault zone. Classic mixing rules are used for defining equivalent heat capacity and thermal conductivity of the saturated medium (see equations 5 and 6 in Guillou-Frottier et al., 2013). Here again, the absolute values of porosity do not greatly influence the hydrothermal regime when compared to the chosen permeability values.

In most models, transient evolution is computed until a steady-state is reached. While initial pressure field always corresponds to a hydrostatic gradient, the initial thermal regime varies from one case to the other, in particular when thermal inheritance is studied (Fig. 5 and 6). When a pure conductive regime is taken as the initial condition, the analytical expression accounting for heat production is applied to the entire model and inserted in the numerical code:

$$T_0(z) = T_0 + \left(\frac{Q_b + A \times H}{k}\right) \times z - \left(\frac{A}{2k}\right) \times z^2 \quad (\text{A5})$$

where T_0 is the imposed surface temperature, Q_b the imposed basal heat flow, A the heat production rate, H the height of the model, k the equivalent thermal conductivity and z is depth from the top surface. By definition, the “temperature anomaly” is defined by the computed temperature minus the equilibrium conductive temperature given in (A5). When a non-conductive state is chosen as an initial condition (e.g. Fig. 7), the obtained solution from a previous run is implemented as the new initial condition.

For the first 2D models (Fig. 1), numerical mesh consists in 6726 triangles, with a maximum size of 20 m. Same mesh parameters have been used for longer models (Fig. 6). For the 3D models, size of tetrahedrals is refined within the fault zone,

down to a maximum size of 100 m for cases with high permeability or with a large fault zone: in the case of Fig. 11 and 14b,
955 the total number of tetrahedras equals 31819, with a maximum size of 100 m within the fault zone.

Within the Comsol Multiphysics™ software, hydrothermal convection equations are solved with an automatically chosen
direct linear solver (e.g. UMFPACK in version 3.5, PARDISO in version 5.4), and time discretization is also automatically
chosen so that absolute and relative tolerance are satisfied. However, in the case of too low tolerance values, several distinct
960 solutions can be obtained when mesh size or the imposed time stepping is modified. To avoid the possibility of getting different
solutions when time stepping or mesh size are modified, relative and absolute tolerances have been set to 10^{-5} and 10^{-6} ,
respectively. This strong constraint allowed getting stable and robust solutions, as confirmed by the 3D benchmark experiments
(Appendix B).

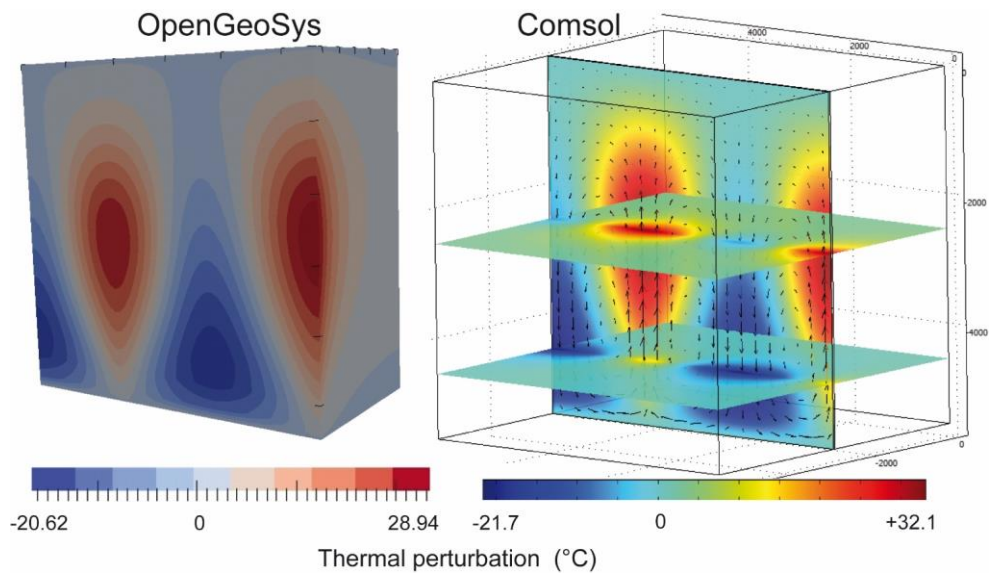
965 **Appendix B: 3D Benchmark tests**

For the 3D benchmark experiments, the same fluid properties as those used in Magri et al. (2017) have been imposed (linear
temperature-dependence for density law, and exponential decrease of viscosity with temperature, see their Fig. 1b and
Appendix A). Rock (fault and host rock) properties are also the same. Transient evolution is computed up to $t_0 + 10^{13}$ s, as in
their Fig. 5. It must be specified that an error appeared in the published results of 2D experiments in Magri et al. (2017):
970 medium permeability was not “ $1.019 \cdot 10^{-13} \text{ m}^2$ ” but around $1\text{-}5 \cdot 10^{-15} \text{ m}^2$ (Magri, pers. comm., 2019). This value allowed us to
reproduce the 2D results (not shown here) including their fluid velocity pattern (their Fig. 3), but with a maximum velocity
value of $1.4 \cdot 10^{-9} \text{ m}\cdot\text{s}^{-1}$ and not $2.8 \cdot 10^{-6} \text{ m}\cdot\text{s}^{-1}$. Similarly, the published 3D result in their Fig. 5 indicates minimum and maximum
temperature perturbations of “ $\pm 32^\circ\text{C}$ ” instead of -20.62°C and 28.94°C (Magri, pers. comm., 2019). The correct temperature
range is given in Fig. B1.

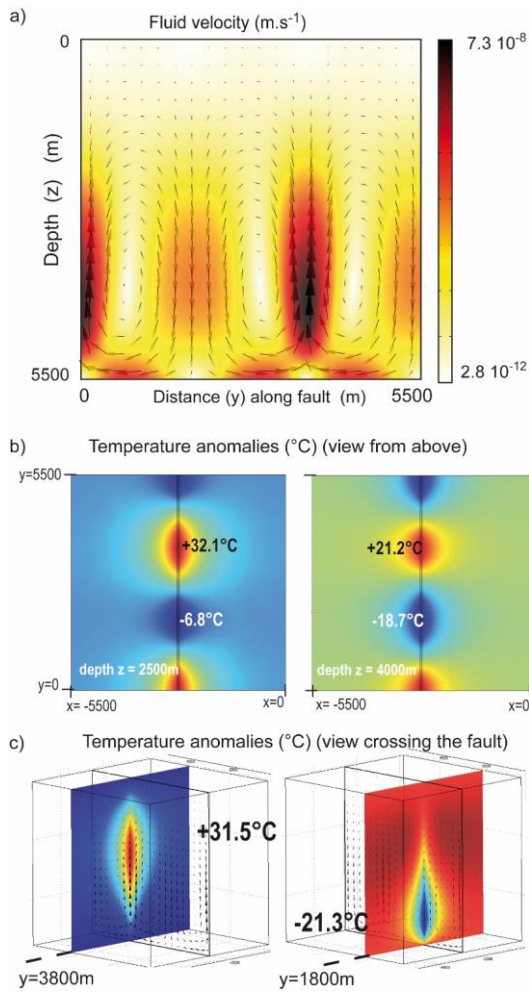
975 Figure B1 shows the 3D benchmark experiment performed with OpenGeoSys (left figure, Magri, pers. comm., 2019) and with
Comsol Multiphysics™ (our study, right figure). All boundary conditions are the same, and geometries are identical (fault
width is 40 m). The results shown in Fig. B1 correspond to time $t_0 + 10^{13}$ s. Convective patterns are identical but temperature
anomalies differ by 1 and 3°C for minimum and maximum values, respectively. As explained by Magri et al. (2017), numerical
980 instabilities may easily develop in density-driven flow problems. In addition, time discretization adopted by Comsol
Multiphysics™ may also differ from that imposed in the other numerical codes.

Figure B2 illustrates some additional details of the convective regime within the fault. Fluid velocity pattern is shown in Fig.
B2a, temperature anomalies viewed from above at different depths are shown in Fig. B2b, and temperature anomalies from
985 sections perpendicular to the fault are shown in Fig. B2c. Interestingly, despite fault width is small (40 m), thermal anomalies

diffuse over hundreds of meters (and even thousands of meters if values different from the conductive regime are accounted for).



990 **Figure B1.** Benchmark experiment for a 40 m wide fault zone embedded in impervious host rock (cube of 5.5 km), as in the Magri et al. (2017) study (left). Our result (right) indicates slight differences in temperature perturbation (see text) but convective pattern is identical.



995 **Figure B2.** Details on the 3D benchmark experiment of Figure B1. a) Field velocity and values within the fault ; b) lateral diffusion of temperature anomalies at depths 2500 and 4000 m ; c) lateral diffusion of hot and cold anomalies, perpendicularly to the fault.

Code availability

The numerical codes are available upon request to the first author.

1000 **Author contribution**

HD, GL_a, AT, VR and GL_i contribute to this work through their PhD theses on fluid circulation in permeable fault zones. HD and LGF developed the 3D model, GL_a implemented the density law. LGF wrote the initial draft and all co-authors contribute to the writing of the final manuscript.

Competing interest

1005 The authors declare that they have no conflict of interest.

Special Issue statement

Acknowledgements

We would like to thank Pr. Fabien Magri for fruitful discussions and for running again his 3D benchmark experiment to answer our questions. This study was partly funded by the Labex Voltaire (ANR-10-LABX-100-01) homed at Orléans University and BRGM, the French Geological Survey, and by the “GERESFAULT” project (ANR-19-CE05-0043). We warmly thank Steve E. Ingebritsen and Fabrice J. Fontaine for their thorough and constructive reviews.

1010

References

- 1015 Achziger-Putančić, P., Loew, S., Hiller, A., and Mariethoz, G.: 3D fluid flow in fault zones of crystalline basement rocks (Poehla-Tellerhaeuser Ore Field, Ore Mountains, Germany), *Geofluids*, 16, 688-710, <https://doi.org/10.1111/gfl.12192> 2016.
- Achziger-Putančić, P., Loew, S., and Hiller, A.: Factors controlling the permeability distribution in fault vein zones surrounding granitic intrusions (Ore Mountains/Germany), *J. Geophys. Res.*, 122, 1876-1899, <https://doi.org/10.1002/2016JB013619> 2017.
- 1020 Agee, J.J.: Fluid flow in the deep crust, *Treatise on geochemistry*, 2nd edition, 203-247, <https://doi.org/10.1016/B0-08-043751-6/03023-1> 2014.
- [Andersen, C., Rüpke, L., Hasenclever, J., Grevemeyer, I., and Petersen, S.: Fault geometry and permeability contrast control vent temperatures at the Logatchev 1 hydrothermal field, Mid-Atlantic Ridge, *Geology*, 43, 51-54, https://doi.org/10.1130/G36113.1 2015.](https://doi.org/10.1130/G36113.1)
- 1025 Artemieva, I.M., Thybo, H., Jakobsen, K., Sorensen, N. K., Nielsen, L.S.K.: Heat production in granitic rocks: Global analysis based on a new data compilation GRANITE2017, *Earth Sci. Rev.*, 172, 1-26, <https://doi.org/10.1016/j.earscirev.2017.07.003> 2017.
- Bächler, D., Kohl, T., and Rybach, L.: Impact of graben-parallel faults on hydrothermal convection – RhineGraben case study, *Phys. Chem. Earth*, 28, 431-441, [https://doi.org/10.1016/S1474-7065\(03\)00063-9](https://doi.org/10.1016/S1474-7065(03)00063-9) 2003.
- 1030 Baietto, A., Cadoppi, P., Martinotti, G., Perello, P., Perrochet, P., and Vuataz, F.-D.: Assessment of thermal circulations in strike-slip fault systems : the Terme di Valdieri case (Italian western Alps), *Geol. Soc. Spec. Pub.*, 299, 317-339, <https://doi.org/10.1144/SP299.19> 2008.
- Bartels, A., Behrens, H., Holtz, F., Schmidt, B.C., Fechtelkord, M., Knipping, J., Crede, L., Baasner, A., and Pukallus, N.: The effect of fluorine, boron and phosphorus on the viscosity of pegmatite forming melts, *Chem. Geol.*, 346, 184-198, <https://doi.org/10.1016/j.chemgeo.2012.09.024> 2013
- 1035 Bauer, J.F., Krumbholz, M., Luijendijk, E., and Tanner, D. C.: A numerical sensitivity study of how permeability, porosity, geological structure, and hydraulic gradient control the lifetime of a geothermal reservoir, *Solid Earth*, 10, 2115-2135, <https://doi.org/10.5194/se-10-2115-2019> 2019.
- 1040 Bense, V. F., Gleeson, T., Loveless, S. E., Bour, O., and Scibek, J.: Fault zone hydrogeology, *Earth Sci. Rev.*, 127, 171-192, <https://doi.org/10.1016/j.earscirev.2013.09.008> 2013.
- Blackwell, D.D., Netragu, P.T., and Richards, M.: Assessment of the Enhanced Geothermal System resource base of the United States, *Natur.Resources Res.*, 15, 283-308, <https://doi.org/10.1007/s11053-007-9028-7> 2006

Code de champ modifié

- 1045 Boiron M.-C., Cathelineau, M., Banks, D. A., Fourcade, S., and Vallance, J. : Mixing of metamorphic and surficial fluids during the uplift of the Hercynian upper crust: consequences for gold deposition, *Chem. Geol.*, 194, 119-141, [https://doi.org/10.1016/S0009-2541\(02\)00274-7](https://doi.org/10.1016/S0009-2541(02)00274-7) 2003.
- Bonnemaison, M., and Marcoux, E.: Auriferous mineralization in some shear-zones: A three-stage model of metallogenesis, *Mineral. Deposita*, 25, 96–104, <https://doi.org/10.1007/BF00208851> 1990.
- 1050 Bonté, D., Guillou-Frottier, L., Garibaldi, C., Bourguin, B., Lopez, S., Bouchot, V., and Lucazeau, F.: Subsurface temperature maps in French sedimentary basins: new data compilation and interpolation, *Bull. Soc. Geol. Fr.*, 181, 377-390, <https://doi.org/10.2113/gssgfbull.181.4.377> 2010.
- ~~Börsing, N., Wellmann, J. F., Niederau, J., and Regenauer-Lieb, K.: Entropy production in a box: analysis of instabilities in confined hydrothermal systems, *Water Resour. Res.*, 53, 7716-7739, <https://doi.org/10.1002/2017WR020427> 2017.~~
- ~~Butler, R.W.H. and Torvela, T.: The competition between rates of deformation and solidification in syn-kinematic granitic intrusions: resolving the pegmatite paradox, *J. Struct. Geol.*, 117, 1-13, <https://doi.org/10.1016/j.jsg.2018.08.013> 2018.~~
- 1055 Clauser, C., and Villinger, H.: Analysis of conductive and convective heat transfer in a sedimentary basin, demonstrated for the Rheingraben, *Geophys. J. Int.*, 100, 393-414, <https://doi.org/10.1111/j.1365-246X.1990.tb00693.x> 1990.
- Cloetingh, S., van Wees, J.D., Ziegler, P.A., Lenkey, L., Beekman, F., Tesaro, M., Förster, A., Norden, B., Kaban, M., Hardebol, N., Bonté, D., Genter, A., Guillou-Frottier, L., TerVoorde, M., Sokoutis, D., Willingshofer, E., Cornu, T., and 1060 Worum, G.: Lithosphere tectonics and thermo-mechanical properties: An integrated modelling approach for Enhanced Geothermal Systems exploration in Europe, *Earth Sci. Rev.*, 102, 159-206, <https://doi.org/10.1016/j.earscirev.2010.05.003> 2010.
- Coumou, D., Driesner, T., Geiger, S., Heinrich, C. A., and Matthäi, S.: The dynamics of mid-ocean ridge hydrothermal systems: splitting plumes and fluctuating vent temperatures, *Earth Planet. Sci. Lett.*, 245, 218-231, 1065 <https://doi.org/10.1016/j.epsl.2006.02.044> 2006.
- Coumou, D., Driesner, T., Geiger, S., Paluszny, A., and Heinrich, C.A.: High-resolution three-dimensional simulations of mid-ocean ridge hydrothermal systems, *J. Geophys. Res.*, 114, B07104, <https://doi.org/10.1029/2008JB006121> , 2009.
- Coelho, G., Branquet, Y., Sizaret, S., Arbaret, L., Champallier, R., and Rozenbaum, O.:...Permeability of sheeted dykes beneath oceanic ridges: Strain experiments coupled with 3D numerical modeling of the Troodos Ophiolite, Cyprus. *Tectonophysics*, 1070 644-645, 138-150, <https://doi.org/10.1016/j.tecto.2015.01.004> 2015.
- Cox, S.F.: The application of failure mode diagrams for exploring the roles of fluid pressure and stress states in controlling styles of fracture-controlled permeability enhancement in faults and shear zones, *Geofluids*, 10, 217-233, <https://doi.org/10.1111/j.1468-8123.2010.00281.x> 2010.
- Curewitz, D. and Karson, J.A.: Structural settings of hydrothermal outflow: Fracture permeability maintained by fault 1075 propagation and interaction, *J. Volcanol. Geotherm. Res.*, 79, 149-168 [https://doi.org/10.1016/S0377-0273\(97\)00027-9](https://doi.org/10.1016/S0377-0273(97)00027-9) 1997.

- Della Vedova, B., Vecellio, C., Bellani, S., and Tinivella, U.: Thermal modelling of the Larderello geothermal field (Tuscany, Italy), *Int. J. Earth Sci.*, 97, 317–332, <https://doi.org/0.1007/s00531-007-0249-0> 2008.
- 1080 Deveaud, S., Guillou-Frottier, L., Millot, R., Gloaguen, E., Branquet, Y., Villaros, A., Pichavant, M., and Barbosa da Silva, D.: Innovative and multi-disciplinary approach for discussing the emplacement of Variscan LCT-pegmatite fields, *Proceedings of the 13th SGA Biennial Meeting, Nancy, France, 24-27 August 2015*, Vol. 2, 717-720, 2015
- Duwiquet, H., Arbaret, L., Guillou-Frottier, L., Heap, M. J., and Bellanger, M.: On the geothermal potential of crustal fault zones: a case study from the Pontgibaud area (French Massif Central, France), *Geotherm. Energy*, 2019, 7-33, <https://doi.org/10.1186/s40517-019-0150-7> 2019.
- 1085 Erkan, K.: Geothermal investigations in western Anatolia using equilibrium temperatures from shallow boreholes, *Solid Earth*, 6, 103-113, <https://doi.org/10.5194/se-6-103-2015> 2015.
- Fairley, J. P., and Hinds, J. J., Rapid transport pathways for geothermal fluids in an active Great Basin fault zone, *Geology*, 32, 825-828, <https://doi.org/10.1130/G20617.1> 2004.
- Faulds, J., Coolbaugh, M., Bouchot, V., Moeck, I., and Oğuz, K.: Characterizing structural controls of geothermal reservoirs in the Great Basin, USA, and western Turkey: developing successful exploration strategies in extended terranes, *Proceedings World Geothermal Congress, Bali, Indonesia, 25-29 April 2010*, 11 p., 2010.
- 1090 Faulkner, D.R., Jackson, C.A.L., Lunn, R.J., Schlische, R.W., Shipton, Z.K., Wibberley, C.A.J., and Withjack, M.O.: A review of recent developments concerning the structure, mechanics and fluid flow properties of fault zones, *J. Struct. Geol.*, 32, 1557-1575, <https://doi.org/10.1016/j.jsg.2010.06.009> 2010.
- 1095 Fehn, U., Cathles, L., and Holland, H.D.: Hydrothermal convection and uranium deposits in abnormally radioactive plutons, *Econ. Geol.*, 73, 1556-1566, <https://doi.org/10.2113/gsecongeo.73.8.1556> 1978.
- Fontaine, F. J., Rabinowicz, M., and Boulègue, J.: Permeability changes due to mineral diagenesis in fractured crust: implications for hydrothermal circulation at mid-ocean ridges, *Earth Planet. Sci. Lett.*, 184, 407-425, [https://doi.org/10.1016/S0012-821X\(00\)00332-0](https://doi.org/10.1016/S0012-821X(00)00332-0) 2001.
- 1100 Fontaine, F.J., and Wilcock, W.S.D.: [Two-dimensional numerical models of open-top hydrothermal convection at high Rayleigh and Nusselt numbers: Implications for mid-ocean ridge hydrothermal circulation](https://doi.org/10.1029/2007GC001601), *Geochim. Geophys. Geosyst.*, 8, Q07010, <https://doi.org/10.1029/2007GC001601> 2007
- Forster, C., and Smith, L.: The influence of groundwater flow on thermal regimes in mountainous terrain: a model study, *J. Geophys. Res.*, 94, 9439-9451, <https://doi.org/10.1029/JB094iB07p09439> 1989.
- 1105 Garibaldi, C., Guillou-Frottier, L., Lardeaux, J.-M., Bonté, D., Lopez, S., Bouchot, V., and Ledru, P.: Thermal anomalies and geological structures in the Provence basin: implications for hydrothermal circulations at depth, *Bull. Soc. Geol. Fr.*, 181, 363-376, <https://doi.org/10.2113/gssgfbull.181.4.363> 2010.
- Gerdes, M., Baumgartner, L. P., and Person, M.: Convective fluid flow through heterogeneous country rocks during contact metamorphism, *J. Geophys. Res.*, 103, 23983-24003, <https://doi.org/10.1029/98JB02049> 1998.

- 1110 Gourcerol, B., Kontak, D.J., Petrus, J.A. and Thurston, P.C.: Application of LA ICP-MS analysis of arsenopyrite to gold metallogeny of the Meguma Terrane, Nova Scotia, Canada, *Gondwana Res.*, 81, 265-290, <https://doi.org/10.1016/j.gr.2019.11.011> 2020.
- Guillou-Frottier, L., Carré, C., Bourguin, B., Bouchot, V., and Genter, A.: Structure of hydrothermal convection in the Upper Rhine Graben as inferred from corrected temperature data and basin-scale numerical models, *J. Volcanol. Geotherm. Res.*, 256, 29-49, <https://doi.org/10.1016/j.jvolgeores.2013.02.008> 2013.
- 1115 Harcouët-Menou, V., Guillou-Frottier, L., Bonneville, A., Adler, P. M., and Mourzenko, V.: Hydrothermal convection in and around mineralized fault zones: insights from two- and three-dimensional numerical modeling applied to the Ashanti belt, Ghana, *Geofluids*, 9, 116-137, <https://doi.org/10.1111/j.1468-8123.2009.00247.x> 2009.
- ~~Horne, R. N., Three-dimensional natural convection in a confined porous medium heated from below, *J. Fluid Mech.*, 92, 751-766, <https://doi.org/10.1017/S0022112079000860> 1979.~~
- 1120 Howald, T., Person, M., Campbell, A., Lueth, V., Hofstra, A., Sweetkind, D., Gable, C.W., Banerjee, A., Luijendijk, E., Crossey, L., Karlstrom, K., Kelley, S., and Philipps, F.M.: Evidence for long timescale (>103 years) changes in hydrothermal activity induced by seismic events, *Geofluids*, 15, 252-268, <https://doi.org/10.1111/gfl.12113> 2015.
- Hutnak, M., Hurwitz, S., Ingebritsen, S. E., and Hsieh, P. A.: Numerical models of caldera deformation: Effects of multiphase and multicomponent hydrothermal fluid flow, *J. Geophys. res.*, 114, B04411, <https://doi.org/10.1029/2008JB006151> 2009.
- 1125 Ingebritsen, S.E., and Appold, M.S.: The physical hydrogeology of ore deposits, *Econ. Geol.*, 107, 559-584, <https://doi.org/10.2113/econgeo.107.4.559> 2012.
- Ingebritsen, S. E., and Gleeson, T.: Crustal permeability: introduction to the special issue, *Geofluids*, 15, 1-10, <https://doi.org/10.1111/gfl.12118> 2015.
- 1130 Jammes, S., Huisman, R.S., and Muñoz, J.A.: Lateral variation in structural style of mountain building: controls of rheological and rift inheritance, *Terra Nova*, 26, 201-207, <https://doi.org/10.1111/ter.12087> 2013.
- Jamtveit, B., Putnis, C.V., and Malthe-Sorensen, A.: Reaction induced fracturing during replacement processes, *Contrib. Mineral. Petrol.*, 157, 127-133, <https://doi.org/10.1007/s00410-008-0324-y> 2009.
- Jaupart, C., and Mareschal, J.-C.: Heat generation and transport in the Earth, Cambridge University Press, 464 p., 2011.
- 1135 Jupp, T., and Schultz, A., A thermodynamic explanation for black smoker temperatures, *Nature*, 403, 880-883, <https://doi.org/10.1038/35002552> 2000.
- Kuhn, M., Dobert, F., and Gessner, K.: Numerical investigation of the effect of heterogeneous permeability distributions on free convection in the hydrothermal system at Mount Isa, Australia, *Earth Planet. Sci. Lett.*, 244, 655-671, <https://doi.org/10.1016/j.epsl.2006.02.041> 2006.
- 1140 Lapwood, E.R.: Convection of a fluid in a porous medium, *Math. Proc. Cambridge Philos. Soc.*, 44, 508-521, <https://doi.org/10.1017/S030500410002452X> 1948.
- Launay, G. Hydrodynamique des systèmes minéralisés péri-granitiques : étude du gisement à W-Sn-(Cu) de Panasqueira (Portugal). PhD thesis, University of Orléans, France, 514 p., <https://tel.archives-ouvertes.fr/tel-02101051> 2018.

- Launay, G., Sizaret, S., Guillou-Frottier, L., Fauguerolles, C., Champallier, R., and Gloaguen, E.: Dynamic permeability related to greisenization reactions in Sn-W ore deposits: quantitative petrophysical and experimental evidence., *Geofluids*, 2019, Article ID 5976545, 23 pages, <https://doi.org/10.1155/2019/5976545> 2019.
- 1145 Lawley, C.J.M., Creaser, R.A., Jackson, S.E., Yang, Z., Davis B.J., Pehrsson, S.J., Dubé, B., Mercier-Langevin, P., and Vaillancourt, D.: Unraveling the western Churchill Province Paleoproterozoic gold metallotect: constraints from Re-Os arsenopyrite and U-Pb xenotime geochronology and LA-ICP-MS arsenopyrite trace element chemistry at the BIF-hosted
- 1150 Meliadine gold district, Nunavut, Canada, *Econ. Geol.*, 110, 1425-1454, <https://doi.org.insu.bib.cnrs.fr/10.2113/econgeo.110.6.1425> 2015.
- Lin, G., Zhao, C., Hobbs, B.E., Ord, A., and Mühlhaus, H. B.: Theoretical and numerical analyses of convective instability in porous media with temperature-dependent viscosity, *Commun. Numer. Meth. Eng.*, 19, 787–799, <https://doi.org/10.1002/cnm.620> 2003.
- 1155 Link, G., Vanderhaeghe, O., Béziat, D., de Saint Blanquat, M., Munoz, M., Estrade, G., Guillou-Frottier, L., Gloaguen, E., Lahfid, A., Melleton, J.: Thermal peak detected in gold-bearing shear zones by a thermo-structural study: a new tool to retrieve fluid flow ?, *Proceedings of the 15th SGA Biennial Meeting, Glasgow, Scotland, 27–30 August 2019, Vol. 1*, 260–263, 2019.
- Linstrom, P.J., and Mallard, W.G.: The NIST Chemistry WebBook : a chemical data resource on the internet, *J. Chem. Eng. Data*, 46, 1059-1063, <https://doi.org/10.1021/je000236i> 2001.
- 1160 López, D. L., and Smith, L., Fluid flow in fault zones: Analysis of the interplay of convective circulation and topographically driven groundwater flow, *Water Resour. Res.*, 31, 1489-1503, <https://doi.org/10.1029/95WR00422> 1995.
- Lopez, T., Antoine, R., Kerr, Y., Darrozes, J., Rabinowicz, M., Ramillien, G., Cazenave, A., and Genthon, P.: Subsurface Hydrology of the Lake Chad Basin from Convection Modelling and Observations, *Surv. Geophys.*, 37, 471-502, <https://doi.org/10.1007/s10712-016-9363-5> 2016.
- 1165 Louis, S., Luijendijk, E., Dunkl, I., Person, M.: Episodic fluid flow in an active fault, *Geology*, 47, 938-942, <https://doi.org/10.1130/G46254.1> 2019.
- Lowell, R.P., Van Cappellen, P., and Germanovich L.N.: Silica Precipitation in Fractures and the Evolution of Permeability in Hydrothermal Upflow Zone, *Science*, 260, 5105, 192-194, <https://doi.org/10.1126/science.260.5105.192> 1993.
- 1170 Magri, F., Inbar, N., Siebert, C., Rosenthal, E., Guttman, J., and Möller, P.: Transient simulations of large-scale hydrogeological processes causing temperature and salinity anomalies in the Tiberias Basin, *J. Hydrol.*, 520, 342-355, <http://dx.doi.org/10.1016/j.jhydrol.2014.11.055> 2015.
- Magri, F., Möller, S., Inbar, N., Möller, P., Raggad, M., Rödiger, T., Rosenthal, E., and Siebert, C.: 2D and 3D coexisting modes of thermal convection in fractured hydrothermal systems - Implications for transboundary flow in the Lower
- 1175 Yarmouk Gorge, *Mar. Petroleum Geol.*, 78, 750-758, <https://doi.org/10.1016/j.marpetgeo.2016.10.002> 2016.

- Magri, F., Cacace, M., Fischer, T., Kolditz, O., Wanf, W., and Watanabe, N.: Thermal convection of viscous fluids in a faulted system : 3D benchmark for numerical codes, *Energy Proc.*, 125, 310-317, <https://doi.org/10.1016/j.egypro.2017.08.204> 2017.
- 1180 Malkovski, V. I., and Magri, F.: Thermal convection of temperature-dependent viscous fluids within three-dimensional faulted geothermal systems: estimation from linear and numerical analyses, *Water Resour. Res.*, 52, 1-13, <https://doi.org/10.1002/2015WR018001> 2016.
- Manning C.E., and Ingebristen, S.E.: Permeability of the continental crust: implications of geothermal data and metamorphic systems, *Rev. Geophys.*, 37, 127-150, <https://doi.org/10.1029/1998RG900002> 1999.
- 1185 McKenna J. R., and Blackwell, D. D., Numerical modeling of transient Basin and Range extensional geothermal systems, *Geothermics*, 33, 457-476, <https://doi.org/10.1016/j.geothermics.2003.10.001> 2000.
- McLellan, J. G., Oliver, N. H. S., Hobbs, B. E., and Rowland J. V.: Modelling fluid convection stability in continental faulted rifts with applications to the Taupo Volcanic Zone, New Zealand, *J. Volcanol. Geotherm. Res.*, 190, 109-122, <https://doi.org/10.1016/j.jvolgeores.2009.11.015> 2010.
- 1190 Melleton, J., Gloaguen, E., Frei, D.: Rare-elements (Li-Be-Ta-Sn-Nb) magmatism in the European Variscan belt, a review, *Proceedings of the 13th SGA Biennial Meeting, Nancy, France, 24-27 August 2015, Vol. 2, 807-810, 2015.*
- ~~Mezon, C., Mourzenko, V. V., Thovert, J.-F., Antoine, R., Fontaine, F., Finizola, A., and Adler, P.M.: Thermal convection in three-dimensional fractured porous media, *Phys. Rev., E97, 013106, https://doi.org/10.1103/PhysRevE.97.013106* 2018~~
- Mezri, L., Le Pourhiet, L., and Burov, E.: New parametric implementation of metamorphic reactions limited by water content, impact on exhumation along detachment faults, *Lithos*, 236-237, 287-298, <https://doi.org/10.1016/j.lithos.2015.08.021> , 2015.
- 1195 Micklethwaite, S., Ford, A., Witt, W., and Sheldon, H. A.: The where and how of faults, fluids and permeability – insights from fault stepovers, scaling properties and gold mineralisation, *Geofluids*, 15, 240-251, <https://doi.org/10.1111/gfl.12102> 2015.
- Moeck, I.S.: Catalog of geothermal play types based on geologic controls, *Renew. Sustain. Ener. Rev.*, 37, 867-882, <http://dx.doi.org/10.1016/j.rser.2014.05.032> 2014.
- 1200 ~~Niederau, J., Wellmann, J. F., and Börsing, N.: Analyzing the influence of correlation length in permeability on convective systems in heterogeneous aquifers using entropy production, *Geotherm. Energy*, 2019, 7-35, https://doi.org/10.1186/s40517-019-0151-6~~ 2019.
- Patterson, J. W., Driesner, T., Matthai, S., and Tomlinson, R.: Heat and fluid transport induced by convective fluid circulation within a fracture or fault, *J. Geophys. Res.*, 123, <https://doi.org/10.1002/2017JB015363> 2018a.
- 1205 Patterson, J. W., Driesner, T., and Matthai, S. K.: Self-organizing fluid convection patterns in an en echelon fault array, *Geophys. Res. Lett.*, 45, 4799-4808, <https://doi.org/10.1029/2018GL078271> 2018b.

- Pepin, J., Person, M., Phillips, F., Kelley, S., Timmons, S., Owens, L., Witcher, J., and Gable, C.: Deep fluid circulation within crystalline basement rocks and the role of hydrologic windows in the formation of the Truth or Consequences, New Mexico low-temperature geothermal system, *Geofluids*, 15, 139-160, <https://doi.org/10.1111/gfl.12111> 2015
- Person, M., Hofstra, A., Sweetkind, D., Stone, W., Cohen, D., Gable, C. W., and Banerjee, A.: Analytical and numerical models of hydrothermal fluid flow at fault intersections, *Geofluids*, 12, 312-326, <https://doi.org/10.1111/gfl.12002> 2012.
- Rabinowicz, M., Boulègue, J., and Genthon, P.: Two- and three-dimensional modeling of hydrothermal convection in the sedimented Middle Valley segment, Juan de Fuca Ridge, *J. Geophys. Res.*, 103, 24045-24065, <https://doi.org/10.1029/98JB01484> 1998.
- Roche, V., Sternai, P., Guillou-Frottier, L., Menant, A., Jolivet, L., Bouchot, V., and Gerya, T.: Emplacement of metamorphic core complexes and associated geothermal systems controlled by slab dynamics, *Earth Planet. Sci. Lett.*, 498, 322-333, <https://doi.org/10.1016/j.epsl.2018.06.043> 2018.
- Roche, V., Bouchot, V., Beccalotto, L., Jolivet, L., Guillou-Frottier, L., Tuduri, J., Bozkurt, E., Oguz, K., and Tokay, B.: Structural, lithological, and geodynamic controls on geothermal activity in the Menderes geothermal Province (Western Anatolia, Turkey), *Int. J. Earth Sci.*, 108, 301-328, <https://doi.org/10.1007/s00531-018-16> 2019
- Saar, M. O., and Manga, M.: Depth dependence of permeability in the Oregon Cascades inferred from hydrogeologic, thermal, seismic, and magmatic modeling constraints, *J. Geophys. Res.*, 109, B04204, <https://doi.org/10.1029/2003JB002855> 2004.
- Scott, S., Driesner, T. and Weis, P.: Geologic controls on supercritical geothermal resources above magmatic intrusions. *Nat Commun* 6, 7837, <https://doi.org/10.1038/ncomms8837> 2015.
- Scott, S., and Driesner, T.: Permeability changes resulting from quartz precipitation and dissolution around upper crustal intrusions, *Geofluids*, 2018, 6957306, 19 p. <https://doi.org/10.1155/2018/6957306> 2018.
- Sibson, R.H.: Implications of fault-valve behaviour for rupture nucleation and recurrence, *Tectonophysics*, 211, 283-293, [https://doi.org/10.1016/0040-1951\(92\)90065-E](https://doi.org/10.1016/0040-1951(92)90065-E) 1992.
- Scibek, J.: Multidisciplinary database of permeability of fault zones and surrounding protolith rocks at world-wide sites, *Sci. Data*, 7, 95, <https://doi.org/10.1038/s41597-020-0435-5> 2020.
- Simms, M. A., and Garven, G.: Thermal convection in faulted extensional sedimentary basins : theoretical results from finite-element modeling, *Geofluids*, 4, 109-130, <https://doi.org/10.1111/j.1468-8115.2004.00069.x> 2004.
- Sonney, R., and Vuataz, F.-D.: Numerical modelling of Alpine deep flow systems: a management and prediction tool for an exploited geothermal reservoir (Lavey-les-Bains, Switzerland), *Hydrogeol. J.*, 17, 601-616, <https://doi.org/10.1007/s10040-008-0394-y> 2009.
- Stober, I., and Bucher, K.: Hydraulic conductivity of fractured upper crust: insights from hydraulic tests in boreholes and fluid-rock interaction in crystalline basement rocks, *Geofluids*, 15, 161-178, <https://doi.org/10.1111/gfl.12104> 2015.
- Sutherland, R. et al., Extreme hydrothermal conditions at an active plate-bounding fault, *Nature*, 546, 137-151, <https://doi.org/10.1038/nature22355> 2017.

- Taillefer, A., Soliva, R., Guillou-Frottier, L., Le Goff, E., Martin, G., and Seranne, M.: Fault-related controls on upward hydrothermal flow: an integrated geological study of the Têt fault system, Eastern Pyrénées (France) *Geofluids*, 2017, 8190109, 19 p. <https://doi.org/10.1155/2017/8190109>
- 1245 Taillefer, A., Guillou-Frottier, L., Soliva, R., Magri, F., Lopez, S., Courrioux, G., Millot, R., Ladouche, B., and Le Goff E.: Topographic and faults control of hydrothermal circulation along dormant faults in an orogen, *Geochem. Geophys. Geosys.*, 19, 4972-4995, <https://doi.org/10.1029/2018GC007965> 2018.
- Tenthorey, E., and Cox, S.F.: Reaction-enhanced permeability during serpentinite dehydration, *Geology*, 31, 921-924, <https://doi.org/10.1130/G19724.1> 2003.
- 1250 Tenthorey, E., and Fitz Gerald, J.D.: Feedbacks between deformation, hydrothermal reaction and permeability evolution in the crust: experimental insights, *Earth Planet. Sci. Lett.*, 247, 117–129, <https://doi.org/10.1016/j.epsl.2006.05.005> 2006.
- Turcotte, D. L., and Schubert, G., *Geodynamics*, Second Edition, Cambridge University Press, 456 p., 2002
- Violay, M., Heap, M.J., Acosta, M., and Madonna, C.: Porosity evolution at the brittle-ductile transition in the continental crust: Implications for deep hydrogeothermal circulation, *Sci. Rep.*, 7, 7705, <https://doi.org/10.1038/s41598-017-08108-5> 2017.
- 1255 Wang, M., Kassoy, D.R., and Weidman, P. D.: Onset of convection in a vertical slab of saturated porous media between two impermeable conducting blocks, *Int. J. Heat Mass Transf.*, 30, 1331-1341, [https://doi.org/10.1016/0017-9310\(87\)90165-7](https://doi.org/10.1016/0017-9310(87)90165-7) 1987.
- Wanner, C., Diamond, L. W., and Alt-Epping, P.: Quantification of 3-D thermal anomalies from surface observations of an orogenic geothermal system (Grimsel Pass, Swiss Alps), *J. Geophys. Res.*, 124, <https://doi.org/10.1029/2019JB018335>
- 1260 2019.
- Watanabe, N., Sakagushi, K., Goto, R., Miura T., Yamane, K., Ishibaashi, T., Chen, Y., Komai, T., and Tsuchiya, N.: Cloud-fracture networks as a means of accessing superhot geothermal energy, *Sci. Rep.*, 9, 939, <https://doi.org/10.1038/s41598-018-37634-z> 2019.
- Weis, P., Driesner, T., and Heinrich, C.A.: Porphyry-copper ore shells form at stable pressure-temperature fronts within dynamic fluid plumes, *Science*, 338, 1613-1616, <https://doi.org/10.1126/science.1225009> 2012.
- 1265 Weis, P., Driesner, T., Coumou, D., and Geiger, S.: Hydrothermal, multiphase convection of H₂O-NaCl fluids from ambient to magmatic temperatures: a new numerical scheme and benchmarks for code comparison, *Geofluids*, 14, 347-371, <https://doi.org/10.1111/gfl.12080> 2014.
- Weis, P., The dynamic interplay between saline fluid flow and rock permeability in magmatic-hydrothermal systems, *Geofluids*, 15, 350-371, <https://doi.org/10.1111/gfl.12100> 2015.
- 1270 Wüstefeld, P., Hilse, U., Lüders, V., Wemmer, K., Koehrer, B., and Hilgers, C.: Kilometer-scale fault-related thermal anomalies in tight gas sandstones, *Mar. Petroleum Geol.*, 86, 288-303, <https://doi.org/10.1016/j.marpetgeo.2017.05.015> 2017.

Code de champ modifié

1275 | Zhao, C., Hobbs, B. E., Mühlhaus, H. B., Ord, A., and Lin, G.: Convective instability of 3-D fluid-saturated geological fault zones heated from below, *Geophysical J. Int.*, 155, 213-220, <https://doi.org/10.1046/j.1365-246X.2003.02032.x> 2003.